EUROPEAN ORGANIZATION FOR NUCLEAR RESEARCH

CERN / SPSC 2000-010
SPSC / P 316
7 March 2000

PROPOSAL

Study of Prompt Dimuon and Charm Production
with Proton and Heavy Ion Beams at the CERN SPS

Collaboration

Laboratoire de Physique Corpusculaire (LPC), Université Blaise Pascal, IN2P3-CNRS, Aubière, France:
A. Baldit, J. Castor, A. Devaux, B. Espagnon, P. Force, F. Manso and P. Saturnini.

Laboratory for High Energy Physics (LHEP), University of Bern, Bern, Switzerland:
K. Borer and M. Hess.

Faculty of Mathematics and Physics, Comenius University, Bratislava, Slovakia:
P. Chochula1), P. Rosinsky and M. Zagiba.

Dipartimento di Fisica dell'Università and Sezione INFN, Cagliari, Italy:
C. Cicalò, A. De Falco, M.P. Macciotta, A. Masoni, G. Puddu, S. Serci, E. Siddi and G. Usai.

CERN, European Organization for Nuclear Research, Geneva, Switzerland:
L. Casagrande, B. Gorini, V. Granata2), E. Heijne, B. Lenkeit, C. Lourenço*), V.G. Palmieri, I. Ropotar3) and P. Sonderegger*,4).

Instituto Superior Técnico (IST), Universidade Técnica de Lisboa, Lisbon, Portugal:
J. Barbosa, P. Ramalhete and J. Seixas.

Institut de Physique Nucléaire de Orsay (IPNO), Université Paris-Sud, IN2P3-CNRS, Orsay, France:
M.P. Comets, D. Jouan, Y. Le Bornec, M. Mac Cormick and N. Willis.

Laboratoire de Physique Nucléaire des Hautes Energies (LPNHE), Ecole Polytechnique, IN2P3-CNRS, Palaiseau, France:
B. Chaurand5) and L. Kluberg5)

Dipartimento di Fisica dell'Università and Sezione INFN, Turin, Italy:
R. Arnaldi, P. Cortese, N. De Marco, A. Musso and E. Scomparin.

Institut de Physique Nucléaire de Lyon (IPNL), Université Claude Bernard Lyon-I, IN2P3-CNRS, Villeurbanne, France:
B. Cheynis, L. Ducroux, E. Gangler, J.Y. Grossiord and A. Guichard.

Yerevan Physics Institute (YerPhI), Yerevan, Armenia:
V. Danielyan, A. Grigorian, S. Grigoryan, H. Gulkanyan, R. Hakobyan, S. Mehrabyan, R. Shahoyan and H. Vardanyan.

---

*) Spokespersons
1) Now at CERN
2) Also at Brunel University, Brunel, England
3) Also at Wuppertal University, Wuppertal, Germany
4) Also at IST, Universidade Técnica de Lisboa, Lisbon, Portugal
5) Personal commitment

Acknowledgements

For the preparation of this proposal, we had very fruitful discussions with R. Divia, F. Formenti, T. Grassi, A. Morsch, L. Musa, T. Niinikoski and G. Stefanini.

Our feasibility tests gained from the enthusiastic participation of M.C. Abreu, C. Baglin, A. Baldisseri, W. Bell, C. Da Via, J. Fargeix, L. Gatignon, J.R. Pizzi, P. Rato-Mendes, P. Sousa and F. Staley.

The help of F. Antinori, J.P. Avondo, F. Bergsma, M. Burns, M. Campbell, E. Cantatore, B. Chadaj, E. Chesi, F. Cossey, J.P. Fabre, C. Ferrari, W. Flegel, Y. Lesénéchal, M. Luptak, B. Mikulec, M. Morel, P. Pierre, J.M. Rieubland and W. Snoeys is also highly appreciated. Special thanks are due to some NA50 institutes (in particular the LIP-Lisbon group) which although not signing this proposal had an important participation in our feasibility tests.

Finally, for their support and encouragement, we are indebted to P. Braun-Munzinger, C. Detraz, A. Drees, L. Foà, G.V. Goggi, U. Heinz, M. Leitch, P. McGaughey, B. Müller, K. Pretzl, E. Quercigh, K. Šafařík, H. Satz, J. Schukraft, E. Shuryak, H.J. Specht and J. Stachel, among many others.

Contents

1 Introduction and Summary

We propose to perform a systematic and accurate measurement of dimuon production, in p-A and heavy ion collisions. The precision of the measurement will allow us to separately study the production of prompt dimuons and the production of muons originating from the decay of charmed mesons.

The basic idea of the experiment is to complement the NA50 muon spectrometer with a completely redesigned target area, using the latest technology in terms of (radiation tolerant) high granularity trackers to access the muon tracks at the vertex level. The availability of radiation tolerant silicon pixel detectors makes it possible to track all the charged particles produced in the heavy ion collision, in the angular acceptance of the muon spectrometer. The measurement of the angle and momenta of the tracks in the new magnetic vertex spectrometer allows to identify among them the two muons which crossed the hadron absorber into the muon spectrometer, giving the trigger. This results in a rather good dimuon mass resolution and in a substantial improvement of the signal to background ratio.

The new detectors, which include a cryogenic silicon microstrip beam detector able to measure the transverse coordinates of each incident ion, will also allow us to measure the impact parameter of the muon tracks, with respect to the interaction point, with a resolution of around 30 μm. Besides considerably improving the rejection of muons from π and K decays, the dominant source of combinatorial background, this “offset” variable is of critical importance to select an event sample highly enriched by semileptonic decays of D mesons. A direct measurement of open charm production in heavy ion collisions becomes possible for the first time. Selecting events where the muon tracks have very small offsets, we can study the production of truly prompt dimuons, as resonance decays, Drell-Yan dimuons and (probe the existence of) thermal dimuons.

These studies will be done as a function of the centrality of the collisions, measured event by event through the multiplicity of charged tracks which come from the same vertex as the muons and, independently, through the forward energy collected in the zero degree calorimeter. This measurement is unbiased by interaction pileup (the factor limiting the luminosity in the NA50 J/ψ measurements), since interactions occuring downstream from the one producing the muon pair are recognized and ignored, while events containing extra upstream interactions are rejected from the analysis.

It is important to situate the goals of this experiment in the present context of heavy ion physics. The study of the phase diagram of strongly interacting matter has justified 15 years of heavy ion physics at the AGS and SPS, and a dedicated collider machine (RHIC) is about to start operation. The SPS experiments have shown strong evidence that a new state of matter is produced in central Pb-Pb collisions at the highest energies. The existing results were discussed in a special workshop in Chamonix [1] in September 1998, were updated in the QM’99 conference [2] in May 1999, and were summarized in a special CERN seminar on February 2000, which was the basis of a Press Release from CERN [3]. In view of the exciting results presently available, further work is needed and justified on the understanding of the critical behaviour of QCD at the SPS energies.

Among the most discussed observations are the centrality dependence of the J/ψ suppression pattern measured by NA50, the low mass dilepton enhancement observed by CERES and the dimuon enhancement observed by NA38/50 and HELIOS-3.

The only data that explicitly show a threshold-like behaviour is the pattern of J/ψ suppression measured by NA50 in Pb-Pb collisions. The current interpretation of these data is that there is a first drop in the J/ψ yield when the collisions reach a (local) energy density above the threshold for melting the χ_c charmonia states, and a second drop when the more tightly bound J/ψ state itself starts melting.

Knowing that the bound $c\overline{c}$ states are suppressed, it is natural to immediately ask what happens to the *unbound* charm. Charm quarks are so heavy that they can only be produced at the earlier stages of the heavy ion collision, before the eventual formation of the QGP state, except if the temperature of the plasma is much higher than currently assumed. *D* meson production also provides the natural reference with respect to which we should study the observed J/ψ suppression, since both production mechanisms depend on the same gluon distribution functions.

The J/ψ suppression pattern in Pb-Pb collisions indicate that the central Pb-Pb collisions produce a state of matter where colour is no longer confined. Now we should move on to the detailed understanding of how deconfinement sets in, and what physics variable governs the threshold behaviour of charmonia (χ_c) suppression: (local) energy density, density of wounded nucleons, density of percolation clusters, etc. This requires collecting data with smaller (and symmetric) nuclear systems like Ag-Ag.

The J/ψ data collected in central Pb-Pb collisions indicate that we are already beyond the point where the phase transition takes place, but do not provide any information on the value of the critical temperature. Finite temperature lattice QCD tells us that the strongly bound J/ψ $c\overline{c}$ state should be screened when the medium reaches temperatures 30–40 % higher than T_c, while the larger and more loosely bound ψ' state should melt near T_c. The NA38 experiment has shown that the ψ' is significantly suppressed when going from p-U to peripheral S-U collisions. We need to see if this suppression follows a smooth pattern or a sudden transition, within a single collision system rather than comparing p-U to S-U data. If the ψ' suppression is due to Debye screening, its suppression pattern could provide a clear measurement of T_c. However, the hadronic "comovers" produced in S-U collisions may "absorb" the ψ' mesons, since its binding energy is only around 40 MeV. What mechanism is responsible for the ψ' suppression? The presently existing results are not clear in what concerns the onset and pattern of the ψ' suppression. A new measurement is needed, with improved mass resolution to have a cleaner separation of the ψ' peak with respect to the J/ψ shoulder, and which scans the energy density region from the p-U to the S-U data. Ag-Ag collisions are also well placed for this study.

Another open question concerning the physics of charmonia production and suppression is the A-dependence of the χ_c mesons, in p-A collisions, which has not been measured and is an important ingredient when interpreting the J/ψ suppression pattern in Pb-Pb collisions, since the radiative decay of the χ_c states leads to 30–40 % of the J/ψ's measured in proton induced collisions. This emphasises the importance of having a good measurement of the A-dependence of the χ_c production cross section, at SPS energies.

Measuring open charm production with displaced vertex muon tracks will also clarify if the enhancement of intermediate mass dimuons is due to the observed simultaneous semileptonic decays of *D* mesons. If the origin of this excess is due to charm enhancement, it makes the J/ψ suppression even more anomalous. If, instead, it is due to thermal virtual photons from the QGP, it becomes the first direct observation of thermal radiation in particle physics.

The understanding of low mass dilepton production will also gain from a more accurate measurement, in terms of statistics, mass resolution and signal to background ratio. In particular, data on the ω and ϕ peaks, down to zero transverse momentum and with a detailed scan in impact parameter, will provide a good reference with respect to which the ρ and “continuum” can be studied.

In summary, our experiment will address several very exciting questions left open by the present SPS heavy-ion programme:

- How does the open charm production cross section evolve as a function of the energy density reached in the collisions? How does it compare to the J/ψ suppression pattern?
- What is the variable (local energy density, cluster density, etc.) that rules the onset of charmonia suppression?
- What is the origin of the ψ' suppression? If it is due to Debye screening (threshold pattern), what is its melting temperature?
- Is the nuclear dependence of J/ψ and χ_c production identical in p-A collisions?
- What is the origin of the dimuon excess seen in the intermediate mass region? Changes in the *D* meson cross section (or kinematics) or production of thermal dimuons?
- Is there a change in the line shape of the short-lived ρ resonance from proton to ion induced collisions? Are there heavy-ion specific features in the ω and ϕ production patterns?

The “exploratory phase” of the heavy ion physics programme at the SPS is over. The final clarification of the present results requires a dedicated study of those specific signals that have already provided very interesting results.

Given the significant contributions that our measurements can bring to the understanding of the presently existing results, we believe that our experiment can play a leading role in building a convincing logical case that establishes beyond reasonable doubt the formation of a deconfined state of matter in heavy ion collisions at the SPS.

This proposal is organized as follows:

The physics motivations of the experiment, as seen in the present context of heavy ion physics, are presented and discussed in Chapter 2. In view of the considerable importance of the measurements we are proposing to perform, it may look surprising that such an experiment has not been proposed before. The reasons for that are made clear in Chapter 3, where we describe the general detector concept and the corresponding technical difficulties. We also present in this chapter the results of the feasibility tests we performed in the last few years, which show that the very recent advent of radiation tolerant silicon pixel detectors and radiation hard cryogenic silicon microstrip detectors finally bring into experimental reach a statistically meaningful measurement of prompt dimuon and open charm production, in the harsh environment of heavy ion collisions.

On the basis of these R&D results, we designed the experimental apparatus presented in detail in Chapter 4, where we describe the beamscope detector and the silicon pixel telescope, besides recalling the main features of the already existing muon spectrometer and zero degree calorimeter. After discussing the detector specific issues, we review the main ideas concerning trigger, data acquisition, and software (online and offline).

We have evaluated the physics capabilities of this experiment with several Monte Carlo simulations, which are presented in Chapter 5 together with the corresponding “physics performance” results. We close the document with the organizational details of the project, in terms of the structure of the collaboration, the sharing of responsibilities and the planning of the future activities. We also detail in Chapter 6 the beam time needed to convert our ideas into a successful experiment.

2 Physics Programme

This chapter briefly reviews the physics motivation of the experiment. The topics are addressed from the lower to the higher dimuon masses: low mass dileptons; ϕ meson; thermal dimuons; open charm; charmonia. The proton-nucleus physics topics are presented at the end of the chapter.

2.1 Low mass dileptons

The CERES experiment has observed that the measured yield of low mass e^+e^- pairs, in Pb-Au collisions, exceeds by a factor of 2.5 the expected signal from hadronic decays in the mass region 0.2–0.7 GeV (see Fig. 2.1). The excess dileptons are concentrated at low p_T and their yield seems to scale with the square of the charged particle multiplicity [1]. Dileptons from $\pi^+\pi^-$ annihilation would increase the expected yield around the mass of the ρ meson, failing to reproduce the measured shape.

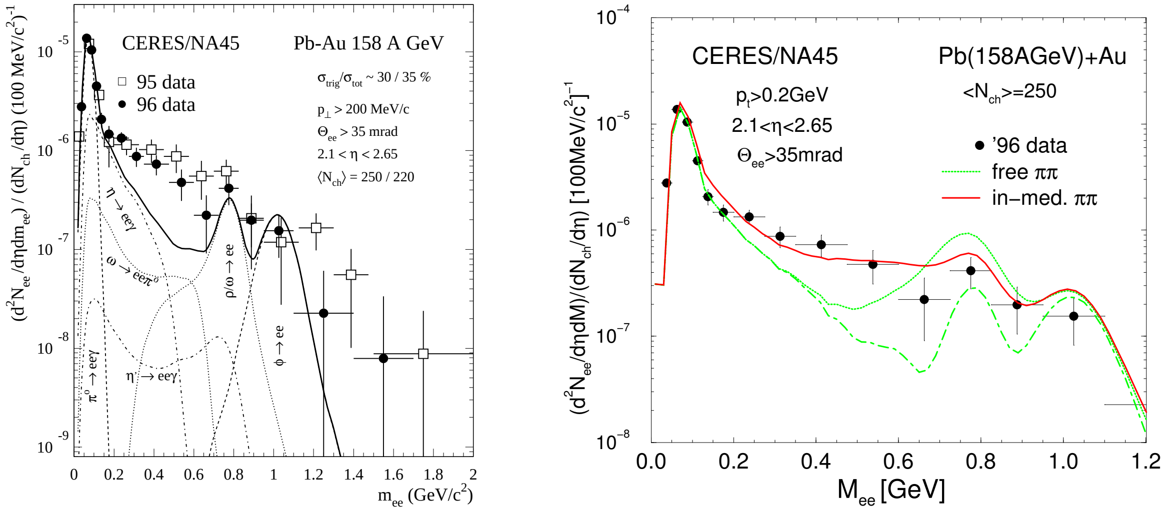

Figure 2.1: Dielectron mass distribution measured by CERES in Pb-Au collisions, compared to the expected hadronic decays (left) and to the contribution from ππ annihilation with and without in medium effects (right).

These observations are consistent with the expectation that the properties of the vector mesons should change when produced in dense matter, due to medium effects. In particular, near the phase transition to the quark-gluon phase, chiral symmetry should be partially restored. As a consequence, vector mesons should become indistinguishable from their chiral partners, inducing changes in the masses and decay widths of the mesons. The short lifetime of the ρ meson, shorter than the expected lifetime of the dense system produced in the SPS heavy ion collisions, makes it a sensitive probe of medium effects and, in particular, of chiral symmetry restoration.

However, to clarify whether or not the observed dilepton enhancement is due to a modification of the vector mesons in the hot and dense medium, we need much more precise measurements of the prompt dilepton mass distributions, as a function of centrality and transverse momentum. Thanks to the highly selective dimuon trigger, the experiment we are proposing is expected to collect (in the final analysis data sample) more than 150 000 ρ, ω and ϕ events per week, with a mass resolution around 20 MeV and a signal to background ratio around 1/4 in the peaks and $\sim$ 1/10 in the continuum (without assuming any enhancement of the signal). Compared to the 1996 CERES measurements, this corresponds to three orders of magnitude larger statistics, two times better mass resolution and about three times better signal to background ratio.

2.2 ϕ meson production

It is well known that strangeness is enhanced in heavy ion collisions. In particular, WA97 has seen [2] that the production rate of the Ω hyperon in central Pb-Pb collisions is enhanced by a factor 15 with respect to the normal behaviour, as defined by the ordinary charged hadrons. Such a strong enhancement is far beyond what could be accommodated by hadronic scenarios, because of the high production thresholds involved. Unfortunately, the enhancement pattern from p-Be to Pb-Pb collisions is not known with sufficient detail. Is there a smooth increase as a function of the number of nucleons participating in the collision, N_{part}, or are there more or less sudden steps, as we see in the case of charmonia production?

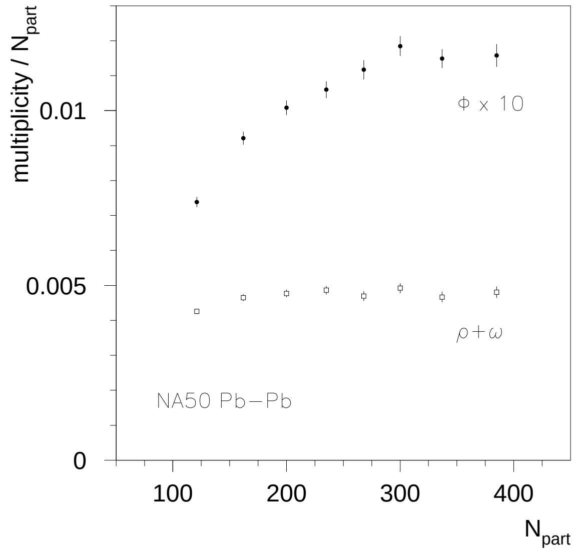

Figure 2.2: Production yield per number of participant nucleons, N_{part}, as a function of N_{part}, for ϕ and $\rho+\omega$ mesons, as measured by NA50.

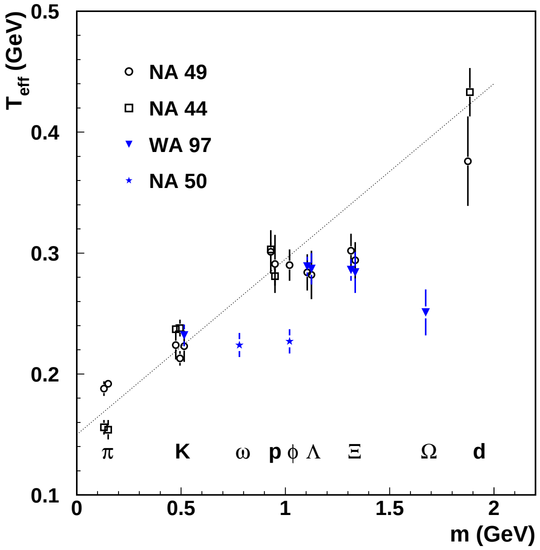

Figure 2.3: Inverse (exponential) slope from transverse mass distributions as a function of the mass of the particles.

The production rate of the ϕ meson can be measured with enough statistics to study strangeness production in many centrality bins, as has been done already by the NA38 and NA50 experiments. Figure 2.2, for instance, shows how the ϕ production yield grows with respect to the $\rho+\omega$ mesons, as a function of centrality [3]. These measurements, however, are limited to the high p_{T} phase space window. The runs optimized for low mass dimuon studies (the so-called

“ϕ setup”), included in the approved NA50 proposal, were sacrificed in view of the beam time needed to clarify the exciting observations concerning the J/ψ suppression. Our new experiment can make this measurement with much better mass resolution, down to zero transverse momentum, and with enough statistics to fully clarify the pattern of strangeness enhancement as a function of the energy density reached in the collisions.

The importance of a measurement down to zero transverse momentum can be understood looking at Fig. 2.3, which shows how the inverse slope of the transverse mass distributions, or “effective temperature”, changes with the mass of the particle, in Pb-Pb collisions. These results were obtained by several experiments, as indicated. In the case of the ϕ we can see that the measurements of NA49 and of NA50 are significantly different (by more than $3\,\sigma$). Given the fact that the phase space window probed by the two experiments is different ($1 < m_\mathrm{T} < 2.2$ GeV in NA49 and $1.5 < m_\mathrm{T} < 3.2$ GeV in NA50), it is not easy to understand if the origin of this difference is related to the different decay channels being probed, $\phi \to K^+K^-$ and $\phi \to \mu^+\mu^-$.

2.3 Thermal dimuons

The search for thermal dimuons as a signature of QGP formation was the original motivation for the NA38 experiment. Searches for this signal were made on the intermediate mass region, between the ϕ and the J/ψ peaks, where it is expected to stand above the other physics sources. Unfortunately, a clear answer could not be found in view of the very high level of combinatorial background present in the data samples. We cannot say that thermal dileptons are emitted in the heavy ion collisions probed by NA38 and NA50. However, we also cannot say the contrary. In fact, it may be that thermal dimuons are the origin of the dimuon enhancement observed [4] in the intermediate mass region (see Fig. 2.4), as defended by Rapp and Shuryak [5].

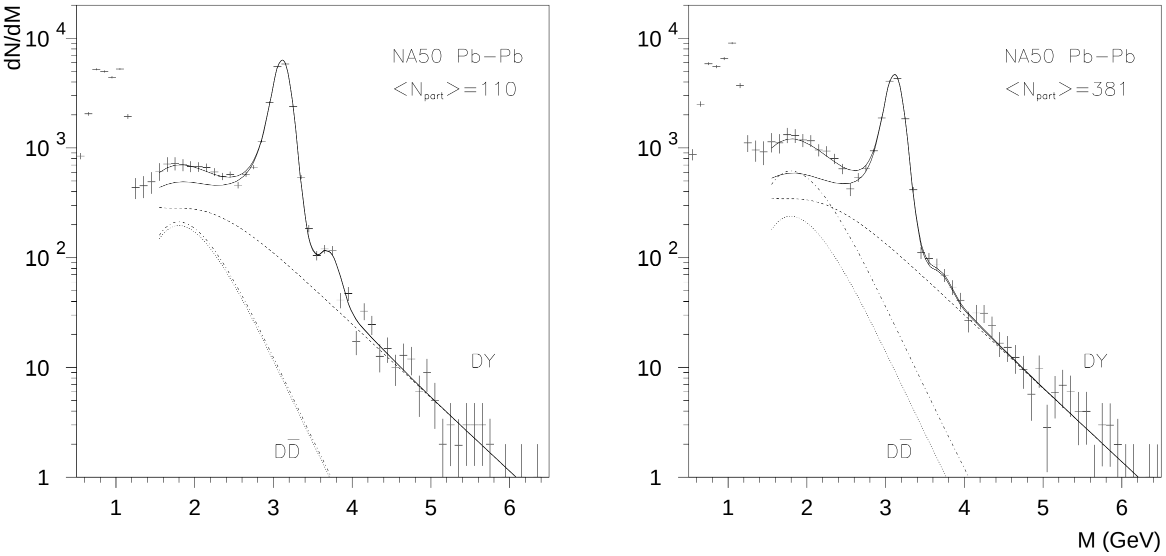

Figure 2.4: Comparison between data and expected sources (solid lines) for peripheral (left) and central (right) Pb-Pb collisions. The $D\overline{D}$ yield has been fixed from the p-A data (lower curve) or left free in the fit (higher curve), properly accomodating the excess.

Once thermal dilepton production becomes measurable, it will provide a new electromagnetic probe through which we can investigate how dense matter is created. Thermal dileptons should be distinguishable from other sources of prompt dimuons through their mass and p_T distributions and through the characteristic dependence of their yield on the multiplicity of charged particles. A correlation with the reaction plane of the collision may help understanding which fraction of thermal dileptons comes from the hadronic phase and which fraction from the QGP.

2.4 D meson production

Charm is the heaviest flavour that can be studied in heavy ion collisions at the SPS energies. The production of charm quarks leads mainly to correlated pairs of D and $\overline{D}$ mesons. Only a few percent of the charmed quark pairs end up in the bound charmonia states presently studied by the NA50 experiment, and which exhibit a rather interesting “anomalous” behaviour. What happens to the vast majority of c quarks? Are they affected by energy loss while crossing the dense (partonic or hadronic) medium? Is charm production enhanced similarly to what has been seen in the strangeness sector?

An exclusive D measurement via hadronic decays is extremely difficult in heavy ion collisions, in view of the small production cross section and of the combinatorial background caused by the very high pion and kaon multiplicities. However, the simultaneous semileptonic decays of (correlated) $D\overline{D}$ pairs lead to a measurable fraction of dileptons, in particular in the mass window between the ϕ and the J/ψ. The superposition of Drell-Yan and $D\overline{D}$ sources is indeed able to properly describe the p-A dimuon data, with cross sections and kinematical distributions derived from exclusive measurements. This is no longer the case for the data collected in heavy ion collisions, as the NA38/NA50 [4] and HELIOS-3 [6] experiments have shown. The measured dimuon continuum can continue to be described by the superposition of these two expected sources, but we must leave the level of the charm contribution increase (linearly with N_{part}) by up to a factor 3 (see Fig. 2.5).

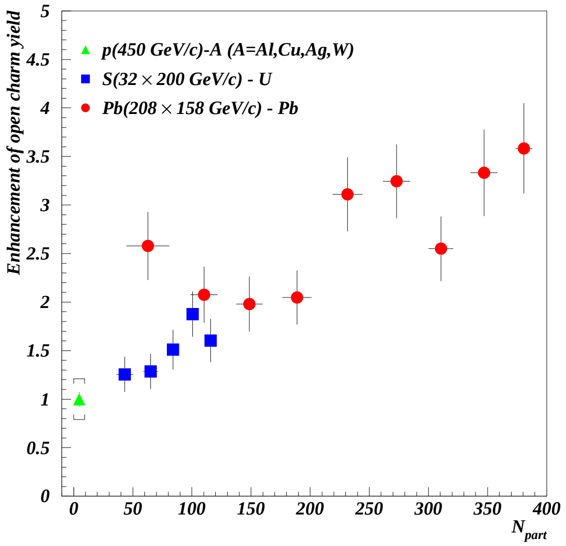

Figure 2.5: Evolution with N_{part} of the factor by which the expected charm yield must be scaled in order to describe the yield of intermediate mass dimuons collected by NA38 and NA50.

In case the “excess” is due to muon pairs from charm decays, it remains to be understood if this is due to a real enhancement of charm production (which would also enhance initial J/ψ

production, making the measured pattern much more anomalous) or if only the kinematical distributions of the *D* mesons are modified by the nuclear medium, leading to a local increase in the acceptance window of the detector. The latter scenario seems to be ruled out by a recent (preliminary) analysis of the NA50 data [7].

Independently of the dimuon enhancement being or not due to charm production, the measurement of open charm will help understanding the J/ψ results. Indeed, both processes are sensitive to the gluon distribution function, while the Drell-Yan process, presently used as reference, is sensitive to the quark and anti-quark distribution functions. In this context, it is worth mentioning that Drell-Yan will not be a useful reference at the high energy colliders, RHIC and LHC.

2.5 J/ψ and ψ′ production and suppression

We know from finite temperature lattice QCD that the strongly bound J/ψ $c\bar{c}$ state should be screened when the medium reaches temperatures around 30 % higher than T_c, the critical temperature for the transition to a partonic medium. The larger and more loosely bound ψ′ and χ_c states could melt at lower temperatures, maybe even at T_c. The NA38 experiment has seen that the ψ′ is significantly suppressed (by about a factor of 2) from p-U to S-U collisions [8]. Since their binding energy is only around 40–50 MeV, the "absorption" of ψ′ mesons by hadronic interactions with other ("comoving") hadrons, also produced in the S-U and Pb-Pb collisions, cannot be completely excluded, making the ψ′ a less unambiguous deconfinement probe than the J/ψ. However, it looks very plausible that the observed ψ′ suppression is actually due to Debye screening, in which case its suppression pattern should exhibit a step at T_c, providing one of the most accurate measurements of this fundamental quantity.

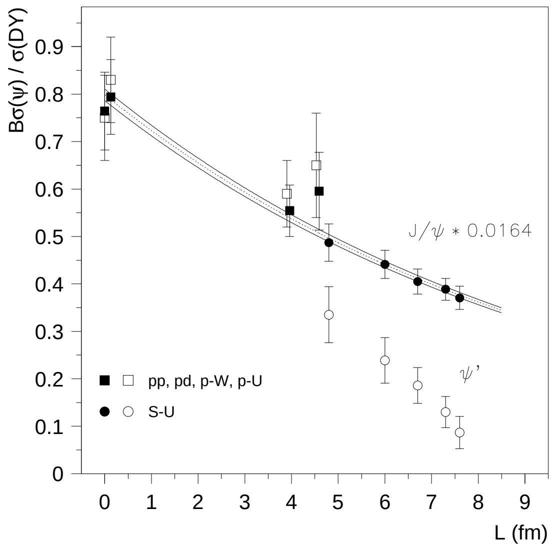

Figure 2.6: ψ′ production yield (open symbols), from p-A to S-U, compared to the "nuclear absorption" of the J/ψ (closed symbols).

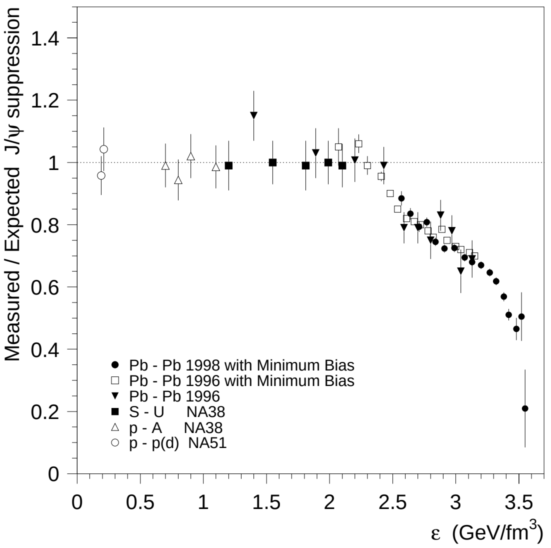

Figure 2.7: Measured J/ψ yield divided by the normal absorption, as a function of the energy density reached in these collisions.

The presently existing results are not clear in what concerns the suppression pattern of the ψ′. Figure 2.6 shows the ratio between the ψ′ and Drell-Yan production rates, as a function of L, the thickness of nuclear matter crossed by the charmonia states. The corresponding J/ψ (normal nuclear absorption) pattern is also shown, scaled down by the factor 1.64 %. Is the "anomalous" ψ' suppression due to melting or to hadronic absorption? A new measurement would be welcome, with improved mass resolution to have a cleaner separation of the ψ' peak with respect to the J/ψ shoulder, and which would scan the region between p-U and S-U. This study would require taking Ag-Ag data, for instance. Such data are also very important to study the evolution with system size of the first drop in the J/ψ suppression pattern (see Fig. 2.7). Indeed, it is possible to predict at which impact parameter, *b*, of Ag-Ag collisions is reached the same threshold in (local) energy density, or any other variable, as reached in Pb-Pb collisions of $b \approx 8$ fm, where the χ_c state starts melting. According to the deconfinement model used in the calculation [9] shown in Fig. 2.8, the onset of anomalous J/ψ suppression is predicted to happen at an impact parameter of 4.4 fm, in Ag-Ag collisions at 158 A GeV. A verification of this prediction would be the final element of proof that the deconfined quark-gluon phase sets in, and would provide fundamental information on the mechanisms behind the observed phenomena.

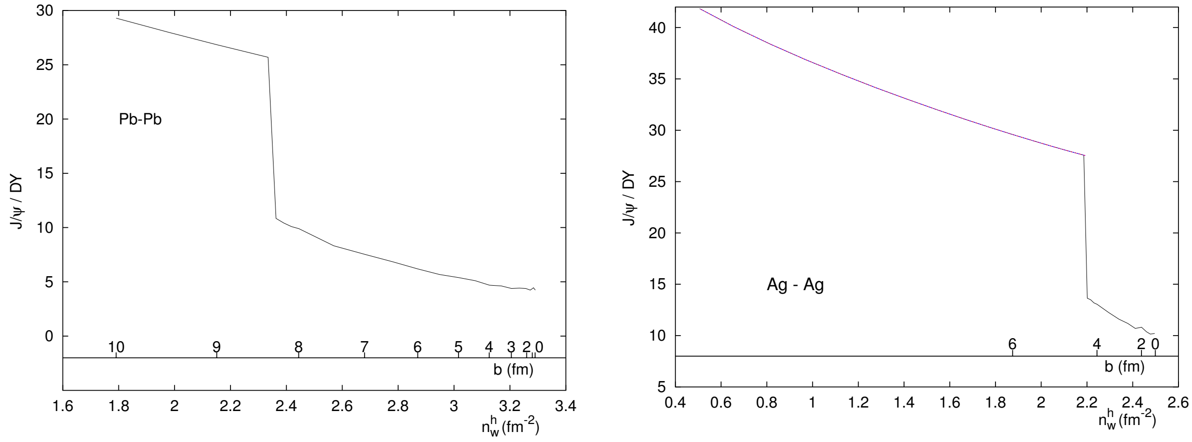

Figure 2.8: Calculated pattern of the anomalous J/ψ suppression in Pb-Pb (left) and Ag-Ag (right) collisions, at 158 A GeV. n_w^h is the density of wounded nucleons.

2.6 Prompt dimuon production in p-A collisions

We will also provide new insight into several issues of dimuon production in p-A collisions. In particular, we will be able to separately study the two main sources of muon pairs contributing to the continuum in the mass window between the ϕ and the J/ψ resonances. A clean measurement of prompt dimuon production at such low masses, covering a broad range in p_{T}, will finally clarify the $q\bar{q}$ annihilation (Drell-Yan) process down to a Q^2 scale close to 1 GeV^2. The sensitivy of this study could be reinforced by running also with π^+ and π^- beams. While charm is mainly produced by gluon fusion, the Drell-Yan cross section is proportional to the squared charge of the annihilating (anti-)quarks. Therefore, the comparison of the dimuon continuum produced with π^+ and π^- beams, on isoscalar targets, should provide complementary information to separate open charm production from $q\bar{q}$ annihilation.

In more general terms, we will be able to investigate if the low mass prompt dimuon continuum can be calculated in next-to-leading-order QCD, and evaluate the importance of higher twist effects. This study can also be done in a sub-sample of high transverse momentum dileptons, for which the QCD calculation is both simpler and more reliable. Furthermore, it has recently been proposed [10] that the study of dileptons with p_T greater than roughly half their mass, mainly produced by subprocesses initiated by gluons, is a good source of information on the gluon momentum density, complementing the complicated studies of inclusive real photon production.

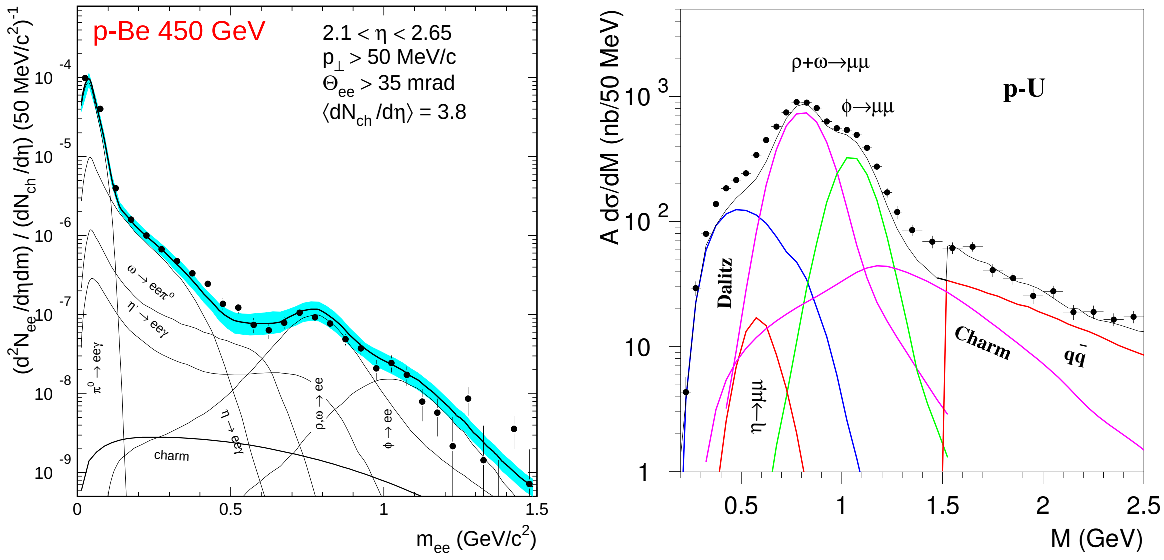

Figure 2.9: Dilepton mass spectra measured in p-Be by CERES (left) and in p-U by NA38 (right) compared to the expected sources. The NA38 data is reduced to the phase space window $m_T > 0.9$ GeV.

In this context we should recall that the low mass dimuon spectrum measured by the NA38 experiment, in p-U collisions, exceeds the sum of the expected sources (the “hadronic cocktail” plus the $D\overline{D}$ decays) by $\sim 40\,\%$ in the mass range 400–650 MeV [11], as shown in Fig. 2.9. The observed excess increases with the dimuon p_T, indicating the presence of a harder source of dileptons in this mass window, possibly related to $q\overline{q}$ annihilation. This hypothesis requires clarification.

2.7 A-dependence of χ_c production

Another promising topic is the measurement of the A-dependence of χ_c production in p-A collisions. It is well known that a big fraction (of the order of 30–40 %) of the hadroproduction cross section of J/ψ mesons is actually due to radiative decays of χ_c mesons. In order to understand the influence of the (hadronic or partonic) matter produced in nuclear collisions on the fate of the *directly* produced J/ψ mesons, we must know what happens to the χ_c contribution. In this sense, it is important to know what is the A-dependence of χ_c production, in proton-nucleus collisions. This question is particularly relevant in view of the “anomalous” J/ψ suppression pattern observed in Pb-Pb collisions by the NA50 experiment [12], which is currently interpreted as indicating that the χ_c states are no longer produced in semi-central Pb-Pb collisions, due to the formation of a state of deconfined matter.

The very recent observation, by the E866 Fermilab experiment [13], using 800 GeV protons on several nuclear targets, that the J/ψ and ψ′ A-dependences are no longer identical for x_F val-

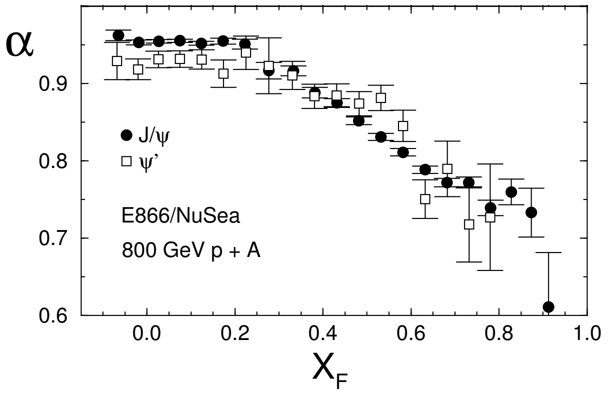

Figure 2.10: Dependence on x_{F} of the α parameter for the J/ψ and ψ' charmonia states, as measured in p-A collisions by the E866 experiment. α is the exponent in the parameterisation $\sigma(p-A) = \sigma_0 \times A^{\alpha}$.

ues below ~ 0.2 (see Fig. 2.10) has stressed the importance of clarifying how the χ_c production is affected by the presence of normal nuclear matter. Measurements of χ_c hadroproduction have been done by a few experiments at Fermilab, in particular by E705 [14] and E771 [15], but no measurements of the A-dependence are available up to the moment.

The proposed experiment may be able to give an important contribution to this physics topic. The main idea is to measure the ratio χ_c to J/ψ, and how this ratio changes from p-Be to p-Pb. As a by product we may get relevant information for the understanding of the basic charmonia production mechanisms (in particular, to help clarifying the validity of the colour octet model).

3 Detector Concept and Feasibility Tests

In this chapter we present the detector concept underlying the experiment we are proposing and the results of the tests we have performed to verify its feasibility.

3.1 Detector strategy

We want to measure as accurately as possible the kinematics of the muons produced in a heavy ion collision. To accomodate the small production cross sections, we need an efficient trigger and fast detectors. The identification of the muon tracks requires a muon spectrometer, with a hadron absorber that only the muons can traverse but which induces multiple scattering and energy loss. To measure the muon kinematics at the vertex level, we need to reconstruct the hundreds of charged particles produced and match them to the muon track.

The rather high track multiplicities lead to problems at the level of occupancies and at the level of radiation tolerance. The first problem can be solved with high granularity detectors, as the silicon pixels used in the WA97 experiment; the second requires radiation tolerant devices, only now starting to become available (the Alice1 pixel readout chip).

The matching between the tracks in the muon spectrometer and the tracks in the vertex spectrometer requires measuring the angle and momenta of the tracks at the vertex with enough accuracy. This means having a magnetic field in the target region and requires a careful optimisation of the muon filter.

In order to significantly distinguish between prompt dimuons and muons from hadronic decays (pions, kaons, D mesons), we need a precise measurement of the interaction point and of the impact parameter of the muon tracks. This requires knowing the transverse position of the incident ions with good accuracy. Silicon microstrip detectors can easily match the required precision in spatial resolution but the radiation dose left by the ion beam being measured would quickly destroy a standard silicon device. Fortunately, this problem can be solved using the recently discovered “lazarus effect”: silicon detectors operated at 130 K can survive huge radiation doses while maintaining their proper functioning, in terms of charge collection efficiency and spatial resolution.

In the remaining of this chapter we will present the results of the feasibility tests we have performed in order to verify that the above problems are solvable with the technology now becoming available. It is clear that the experiment we are proposing would be impossible to perform with the previous generation of particle detection technology. In particular, the pixels closer to the beam line will integrate a radiation dose comparable to running the inner layers of a LHC pp experiment for several years. In what concerns the beamscope detector, it is expected to integrate a dose of $\sim$100 Grad per month, surely a record value that no LHC detector will match.

3.2 Track reconstruction and matching

We have assembled a test pixel telescope consisting of four planes, whose detecting area covered half of the azimuthal acceptance of the muon spectrometer, corresponding to the 3 top sextants.

A total of 33 LHC1 pixel chips were used, according to the layout illustrated in Fig. 3.1. The pixel planes were placed inside the dipole magnet (TC8) that will be used in the real experiment.

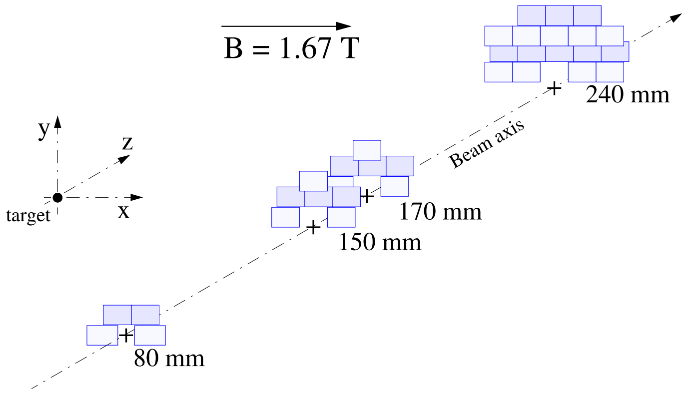

Figure 3.1: Schematic view of the silicon pixel telescope used in the 1998 test runs. These four top-half planes contain 33 chips of 2048 channels each.

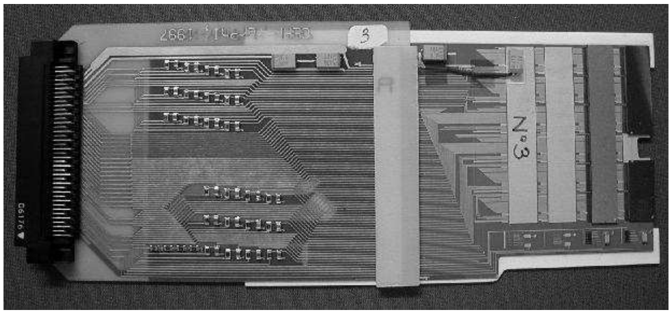

Figure 3.2: Half-plane (of plane 2) assembled for the test pixel telescope.

In what concerns bussing and support, we modified the system developed by WA97, to fit the geometry dictated by the narrow magnet gap (8 cm). Figure 3.2 shows a photograph of one array assembled for the test telescope. The pixel detectors were glued on a ceramic and connected to the bus lines via wire bonding. The ceramic/bus and the kapton cable were mounted on a common support, shaped in such a way that no extra material was present in the acceptance window. The small “wings” on each side of the bus allowed the planes to slide in the mechanical frame that housed the telescope.

The mechanical frame was fixed to a movable support structure inside the TC8 magnet (see Fig. 3.3), which also supported the target and the anti-halo (AH) scintillator counter. This detector was used at the beginning of the run for the steering of the low intensity beam and as safety system during the run (the beam was stopped if the number of counts exceeded a certain threshold).

3.2.1 p-Be collisions

A first feasibility test was performed in April 1998, when we tested our vertex spectrometer with 3 days of 450 GeV protons. In order to increase the acceptance for low-mass dimuons, two changes were done in the muon spectrometer configuration with respect to the standard running conditions of the NA50 experiment. We removed the 80 cm of iron from the end of

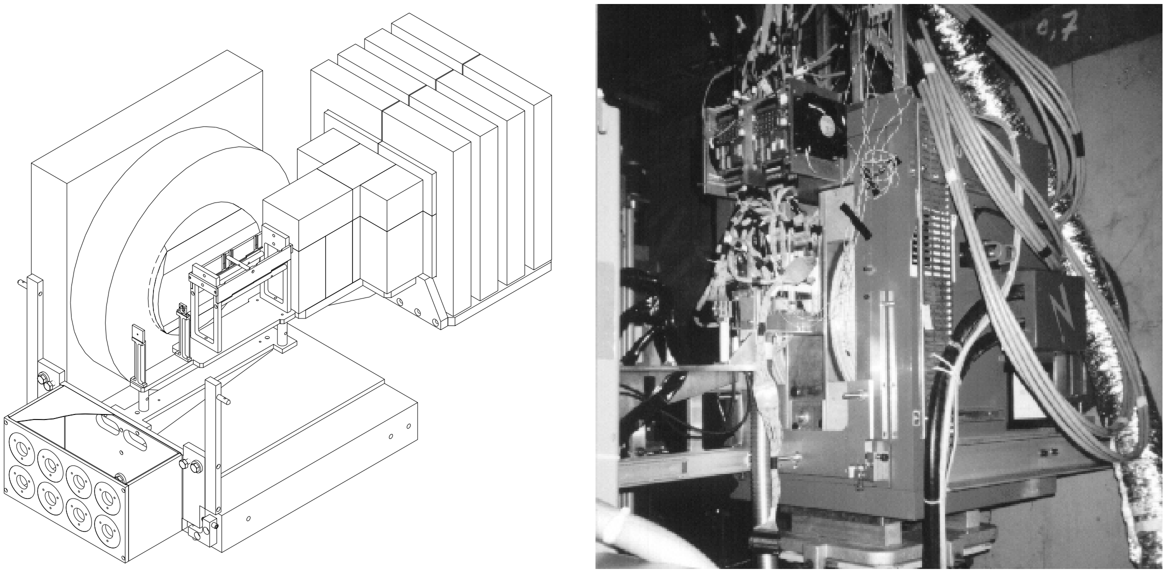

Figure 3.3: Schematic drawing of the layout used in the 1998 test runs (left) and photo of the experimental area (right). The drawing shows, along the beam, the halo counter, the target, the support box of the pixel planes, and the first section of the hadron absorber.

the muon filter, and decreased the current in the toroidal magnet from 7000 A to 3000 A. Since only half of the azimuthal coverage of the muon spectrometer was equipped with pixel planes, the trigger was modified to select only muon pairs crossing those three sextants. The pixel data were read out and stored by a stand-alone DAQ system, and was merged with the muon spectrometer data at the offline level. A small fraction of bursts (less than 1 %) were excluded from the data analysis because of inconsistencies in the two data streams.

The intensity of the proton beam varied between 5×10^7 and 10^8 protons per 2.5 s burst. We used a single beryllium target of 10 mm lenght (about 5 % of λ_{int}) and 12 mm diameter. The corresponding maximum event rate was around one interaction every 500 ns. The readout strobe width was set to 400 ns, except for the first plane where the good timing of the chips allowed the use of a 160 ns strobe, reducing the number of spurious hits. The trigger rate was around 10 to 50 triggers per burst. Alignment runs were also taken, with a single muon trigger, no field in the vertex magnet and at lower beam intensity (around 10^7 protons per burst). The final alignment of the pixel detectors reached a precision of around 5 μm in y (smaller pixel size) and 10 to 20 μm in x (larger pixel size).

The pixel detectors were cooled by means of dry air blown from the bottom of the mechanical frame and the temperature was monitored via PT100 resistors glued directly on the back of the pixel chips (one per plane). At the beginning of the run, with a power consumption of about 100 mW per pixel chip, the temperature was measured to be around 20 °C. Both the power dissipation in the pixel chips and the bulk leakage current of the sensors increased during the run, due to radiation damage. Sometimes, the increased temperature induced thermal “runaway” in some pixel chips, which could be cured by switching them off for a few minutes. The efficiency of the pixel planes deteriorated during the run as the radiation dose increased. The individual channel timing was lost after a few krad. After about 10 krad the chips of the first plane started to suffer from the inhomogeneous irradiation, i.e. the leakage current generated in the sensor could not be compensated over the whole sensitive area of the chips.

The tracks in the muon spectrometer were reconstructed using a modified version of the

NA50 software, to take into account the dipole field at the vertex and the different absorber configuration. Tracks passing through the magnet coils or not pointing to the target were rejected. The tracks in the vertex telescope were reconstructed fitting the hits with a straight line in x and a parabola in y. Tracks with large fitting χ^2 or large offsets at the vertex were rejected.

The track matching procedure selected, among all the tracks reconstructed in the pixel spectrometer, the best candidates to match the two muon tracks. The matching was based on the comparison of the slopes and curvature of the tracks as measured in the two spectrometers. The best candidate tracks were fitted again in the pixel spectrometer after imposing a common vertex and constraining the momenta to the (more accurate) values measured in the muon spectrometer.

The number of good events was very small because of the limited geometrical coverage and low detector efficiency. The last plane was only $\sim 75\,\%$ efficient since the beginning, due to problems of bump bonding, and the efficiency of the first plane decreased significantly during the run, because of the radiation damage. As a result, most of the tracks in the vertex region had only three hits (missing either the first or the last plane) and their lower momentum resolution affected the matching efficiency.

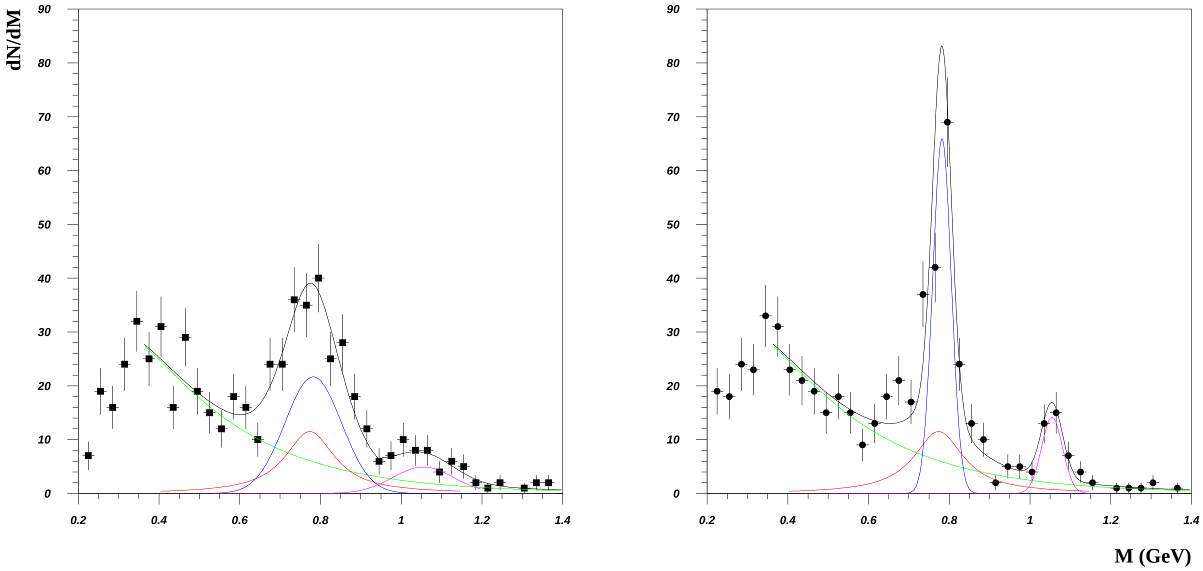

Figure 3.4: Dimuon mass distribution for p-Be collisions before (left) and after (right) using the pixel telescope information. The curves are normalized to the same number of events in both figures.

About 600 opposite-sign dimuon events were correctly reconstructed and matched. Figure 3.4 shows the corresponding dimuon mass spectrum before and after using the pixel spectrometer information to fit the tracks. The data points are compared to the superposition of the ρ (Breit-Wigner), ω and ϕ (gaussian) line shapes, with relative normalisations imposed from previous measurements (equal cross sections for the ρ and ω mesons and 20 times less ϕ's). A clear improvement can be seen in mass resolution, from 70 to 23 MeV σ, as expected.

3.2.2 Pb-Pb collisions

A more challenging feasibility test took place in November 1998, when the pixel vertex spectrometer was exposed for 3 days to the 158 A GeV Pb beam. We used three 1.5 mm thick Pb targets and a maximum beam intensity of $\sim 5 \times 10^6$ Pb ions per 4.5 s burst. With respect to the proton run, 20 cm of iron were added at the end of the hadron absorber. A 3×3 cm^2 scintillator counter, with a 7 mm diameter beam hole, was installed just after the target, to complement the ZDC in the (offline) rejection of events with no interaction in the target. The alignment used low multiplicity Pb-Pb events and special runs collected with a secondary proton beam. The layout of the pixel telescope was basically unchanged, except for the replacement of the damaged first plane and the addition of a similar plane at 9 cm from the target, to introduce some redundancy. To improve the cooling, the frame that supported the pixel planes was closed at the bottom and at the top, except for apertures in correspondence of the pixel planes, forcing the cold air to flow close to the detectors.

A new readout and DAQ system was developed to cope with the higher data flow ($\sim$ 10 kByte per event) and the higher trigger rate ($\sim$ 2000 triggers per burst). The pixel readout cards were modified to use the VME block transfer mode. The new readout system, based on the RIO2 VME on-board processor, could read up to 5000 triggers per burst. Figure 3.5 shows the vertex distribution reconstructed using the tracks in the pixel telescope. The three sub-target positions are clearly distinguishable.

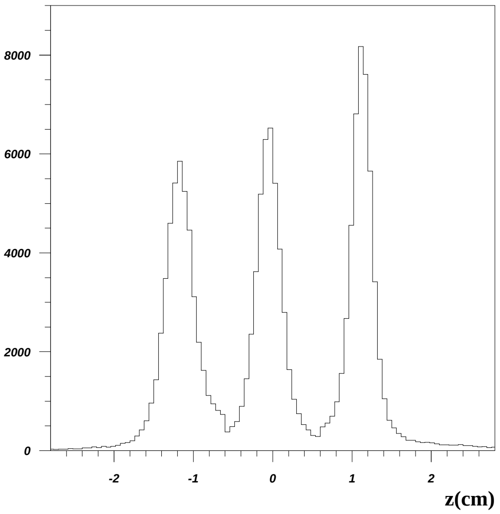

Figure 3.5: Vertex distribution reconstructed from the Pb-Pb events collected in 1998.

All the planes of the telescope suffered from the radiation dose, which resulted in a somewhat lower detection efficiency and, more seriously, also shortened the signal delays in the pixels, so that hits were no longer recorded with their corresponding events. Out of $\sim$ 200 000 opposite-sign muon pairs reconstructed in the muon spectrometer only around 4000 could be matched with tracks reconstructed in the vertex spectrometer. Nevertheless, positive results were achieved at the level of single muon track matching, as can be seen in Fig. 3.6. This figure compares the measured single muon track matching (top row) with the expected performance of the test spectrometer (bottom row), simulated taking into account the measured detector efficiencies. The left plots show the difference between the track slopes measured in the $y-z$ plane by the vertex telescope and by the muon spectrometer. Similar results were obtained for the $x-z$ plane. The central plots illustrate the quality of the matching in terms of track curvature and the plots on the right compare the final matching χ^2, obtained in the measured data and in the simulation. The shapes of the distributions do not reveal any pathology in the matching procedure, and the number of matched muons in the data agrees well with the expectations. Therefore, the

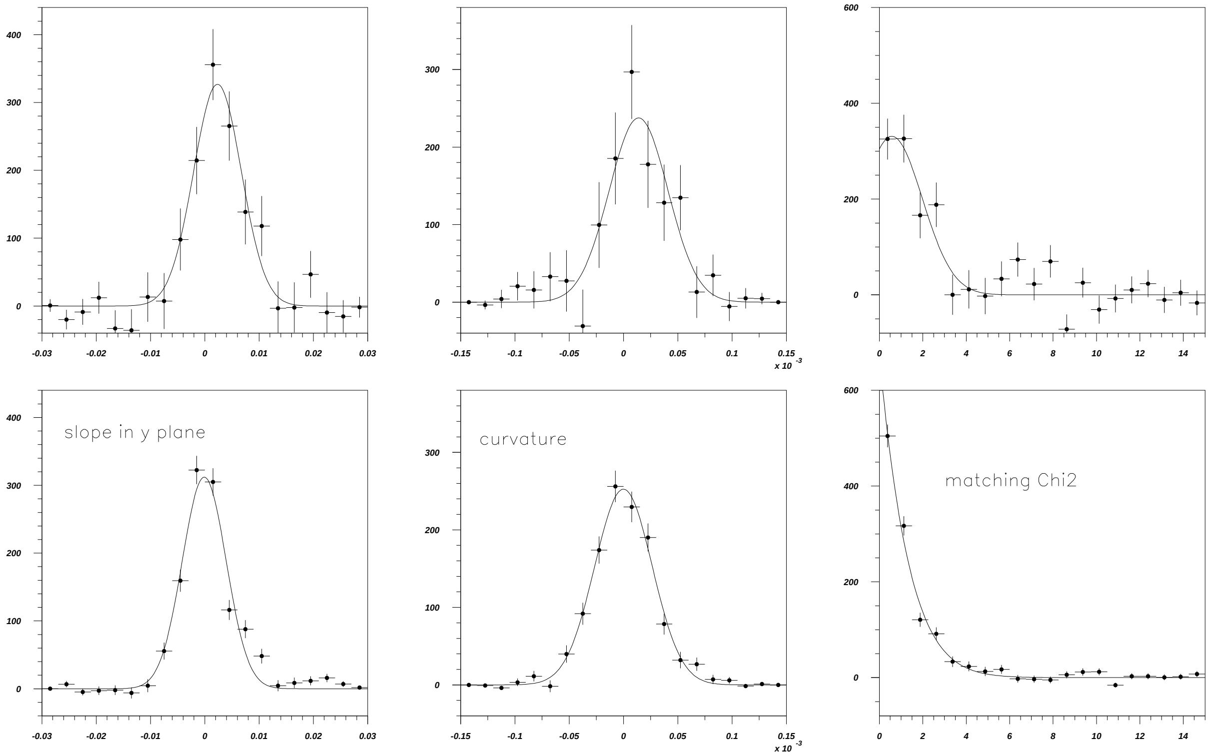

Figure 3.6: Comparison between the measured (top) and simulated (bottom) single muon matching parameters.

track matching procedure seems to also work well in Pb-Pb collisions, with efficiencies that can be realistically estimated by simulation.

3.3 Radiation tolerance of the pixel readout chips

Although the LHC1 pixel readout chip fulfilled our requirements in terms of granularity and time resolution, it was far from tolerating the radiation levels of our experiment. The performance of CMOS electronics is affected by the charge accumulated in the oxides, induced by ionising radiation, which critically depends on the oxide thickness. If enough radiation induced charge is accumulated in the oxide, leakage current can flow from the source and the drain of the transistors, and between transistors. Eventually the transistor can not be switched off, also increasing the overall power consumption. The LHC1 chip was manufactured in a commercial 1 μm CMOS technology. Apart from the results obtained during our feasibility tests, we have also performed a dedicated irradiation test with a β source. After $\sim$10 krad the chip already had a few dead or noisy pixels, and became not functional after about 30 krad. The power consumption in the chip increased by a factor 3.

In the framework of the ALICE experiment, a prototype pixel chip, named Alice1Test, was designed and produced in a commercial 0.5 μm CMOS technology. The electronics was hardened by designing the transistors in “enclosed geometry” and introducing proper guard-ring structures to prevent inter-transistor leakage [1]. The chip was a matrix of 65×2 cells of size 50×420 μm, each cell containing a pre-amplifier, a comparator with adjustable threshold and a data flip-flop. A leakage current compensation circuit as well as a mask flip-flop were also present. The pixels could be tested through an analog pulse injected at the pre-amplifier input. The leakage current compensation was individual for each cell, an improvement with respect to the common compensation of the LHC1 chip. This feature is important if the dose is not homogeneous along the chip (as in our experiment). The radiation tolerance of the chip was measured with different irradiation sources, and the circuit performance started to deteriorate after 600 krad to 1.7 Mrad depending on the type of radiation. We tested one chip behind the NA50 target, where it was exposed mainly to electrons of energy above 1 MeV. A clear degradation of the device performance started after 1.7 Mrad. This dose was measured with a dosimeter placed close to the chip and reproduced with a GEANT simulation.

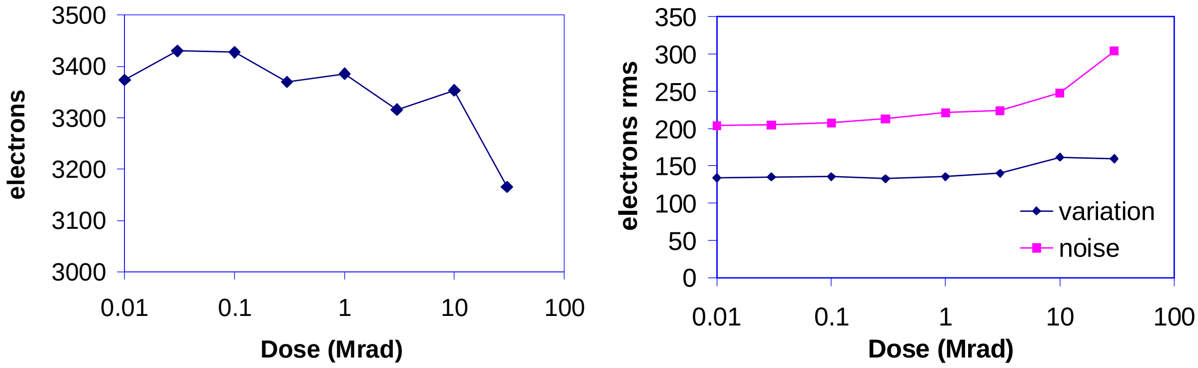

Figure 3.7: Evolution with total dose of the average pixel threshold (left) and of the average and spread of the pixel noise (right), for the Alice2Test prototype.

A further step was made with the design and production of the Alice2Test prototype chip [2], manufactured in 0.25 μm CMOS technology. With respect to the previous prototype, the pixel cell included a delay line and an individual 3-bit fine adjust of the comparator threshold. A minimum threshold of $\sim$1500 electrons could be achieved with a spread of 160 e^- rms in the 135 channels. Besides the X-ray irradiation, we also tested this prototype chip in the NA50 beam line, this time focusing the 450 GeV proton beam directly on the chip. Both irradiation tests confirmed that no relevant changes in the circuit performance could be detected after an integrated dose of 30 Mrad. This can be seen in Fig. 3.7, which shows the evolution of the pixel threshold and of the noise as a function of the dose.

3.4 Tracking the Pb ions

A prototype beamscope detector was built and tested [3], in a joint effort with the RD39 collaboration, with 40 A GeV Pb ions in November 1999, in the NA50 experimental area. A photograph of the installation is shown in Fig. 3.8. The tested detector was very similar to the one we intend to use in the real experiment, and many details are given in the next chapter.

Figure 3.9 shows the design of the Al/p$^+$/n/n$^+$/Al microstrip sensor. The p$^+$-side has 24 narrow strips of 5.135 mm length, with 50 μm pitch and 15 μm width in the central region, plus 4 large strips of the same length with 500 μm pitch and 450 μm width on each side of the central region, and one active guard ring. The simple DC coupled design required only two masks in the production procedure thus reducing significantly the processing cost.

We used two stations, each of them composed by two sensors, mounted back to back on the PCB and with the strips perpendicular to each other. The readout electronics developed for this

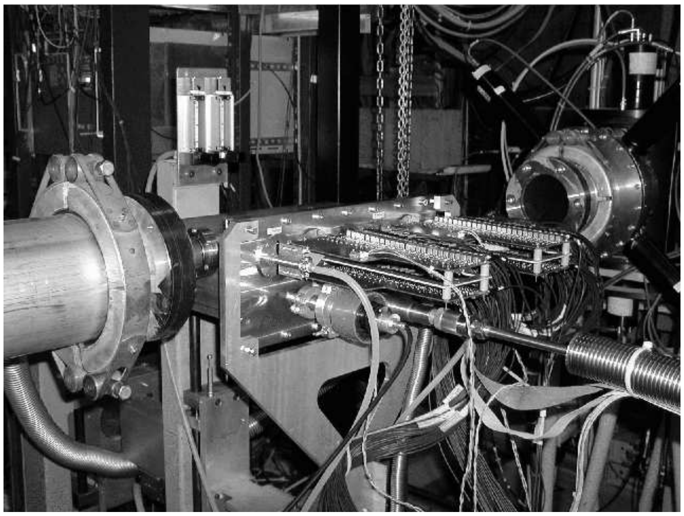

Figure 3.8: The beamscope installed upstream of the NA50 target.

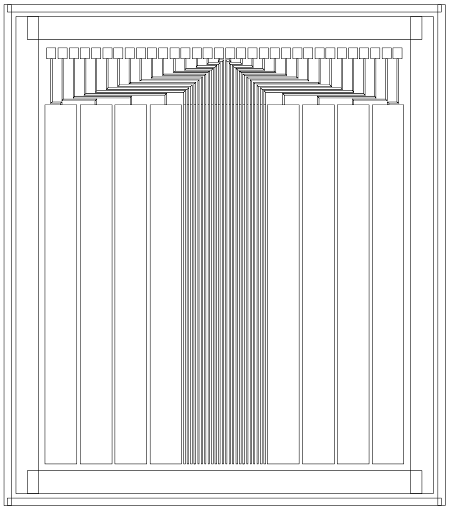

Figure 3.9: Design of the beamscope microstrip sensor.

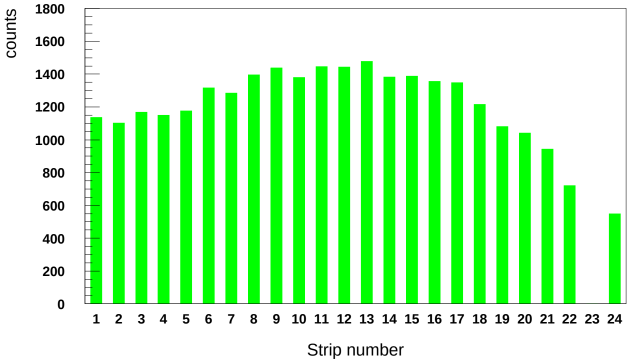

Figure 3.10: The horizontal profile of the SPS ion beam as seen by one plane of the beamscope. The strip pitch is 50 μm. The 23rd strip was defective.

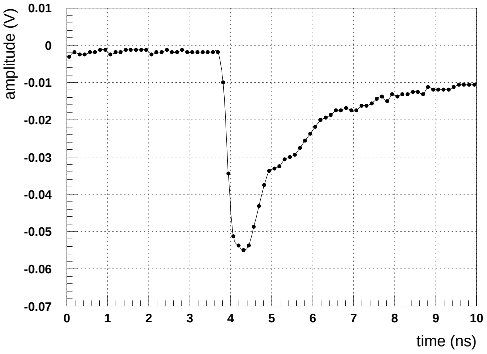

Figure 3.11: Backplane analog signal, for 50 V detector bias, acquired at 8 GS/s.

test will also be used in the real experiment. Online monitoring based on scaler data was used for beam steering. Figure 3.10 shows the measured horizontal beam profile.

The backplane signal was high enough (up to 200 mV for 200 V bias voltage) to be read even without preamplifiers. Figure 3.11 shows one pulse registered on the backplane of one sensor, acquired directly at 8 GS/s, for 50 V detector bias. The short rise time (< 5 ns) is dominated by the readout electronics. We also introduced a shaping stage which reduced the tail. Clearly, this backplane signal can be used for triggering purposes.

Preliminary offline analysis indicates good data quality and a good overall behavior of the beamscope during this test run. We were able to detect and identify each incoming Pb ion up to a beam intensity of $\sim 5 \times 10^7$ ions/burst. The cluster size analysis confirms that a resolution of ~ 20 μm can be achieved. The distribution of delays between the crossing of a Pb ion on a silicon detector and the arrival of the ZDC trigger is shown in Fig. 3.12, with 1.7 ns wide time bins. Notice that the ZDC timing is accurate to within ~ 1 ns (see Fig. 4.9 on page 33). The very precise timing indicated by the narrow peak can be used for an efficient selection of beam particles. A good correlation between strip hits is shown in Fig. 3.13. The deviation of

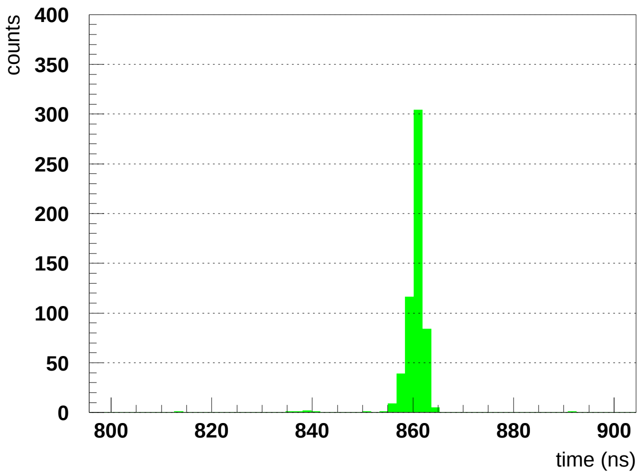

Figure 3.12: Time distribution of the hits in one microstrip detector, with respect to the time of the ZDC triggers.

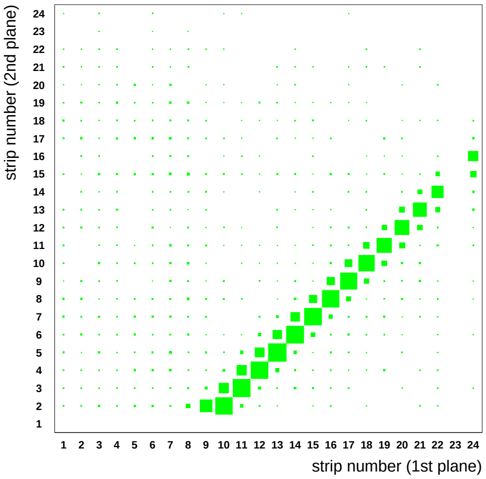

Figure 3.13: Correlation between the hit strips of the two Y planes.

the diagonal with respect to the origin reveals a misalignment between detector planes 1 and 2 of about 500 μm across 20 cm. During this test, the detectors received a total dose of $\sim$1 Grad and showed no sign of deterioration of the signal. Since the bias voltage can still be increased by a factor 10 and the signal to noise would remain acceptable with signals 10 times smaller, we expect the system to remain operational up to $\sim$100 Grad. This will be verified in a test this year.

4 Experimental Apparatus

In this chapter we describe the apparatus, triggering and data acquisition of the experiment we are proposing.

4.1 The beamscope

The beamscope consists of 2 stations (Beam In 1 and 2) of silicon microstrip detectors placed upstream of the target, each composed of an x and a y plane, and one silicon pad detector (Beam Out) placed downstream of the target. The detectors are centered on the beam axis and are operated at 130 K to take advantage of the Lazarus effect [1]. The microstrip detectors measure the transverse coordinates of each incoming lead ion, providing a strict constraint in the determination of the interaction point, relative to which the offset of the muon tracks will be determined. The comparison of the amplitude information from the analog signal pulses measured in the detectors before and after the target, allows identifying the fraction of events in which a Pb ion has interacted.

All beam detectors are mounted on specially designed PCB's (described below), and installed together with the target inside a vacuum tube. The tube is mounted on a sliding support, which also holds the pixel telescope, and which enters inside the vertex dipole magnet. For the cooling, our baseline option is the open-cycle cooling system based on liquid nitrogen (the same that we used in the November 1999 test). We are currently investigating the possibility of using cryocoolers, which would considerably simplify the maintenance.

The beamscope system consists of a vacuum chamber on which is inserted a top flange equipped with access ports for the detector modules, ports for a LN2 transfer line and additional ports for instrumentation connections. The temperature of the detectors is controlled by adjusting the nitrogen flow and the power dissipated by heaters placed on the PCB's.

The Beam In detectors are placed at 30 cm and 10 cm upstream of the target. Figure 4.1 shows the two detectors placed inside the beam pipe, as well as the associated readout electronics, with 24 channels per plane.

Each station is composed by an x and a y plane of 24 single-sided, DC coupled, 50 μm pitch silicon microstrips. The sensor design is very similar to that of the prototype, including the 4 large strips (500 μm pitch) on each side. The main differences consist in the increase of the strip length from 5.1 to 12 mm and the addition of perpendicular strips at the far edge. In this way, we can have a very low intensity and defocused Pb beam passing at the same time through the beamscope strips and the pixels of the vertex spectrometer closest to the beam axis. This will allow on-line alignment between the two systems. A precise sensor geometry is created at the short sides of the strips, and a well-defined decrease to zero of the electrical field is obtained at the edge of the silicon chip.

The detector module, shown in Fig. 4.2, is a printed circuit board made of 6 copper layers separated by glass-epoxy. The glue used to attach the different layers is resistant to thermal shocks at low temperatures and has a high thermal conductivity. The layers are designed so that the thermal conduction between the flange and the sensors is low, whereas the transverse conduction is improved by the patterning of the ground metal layers.

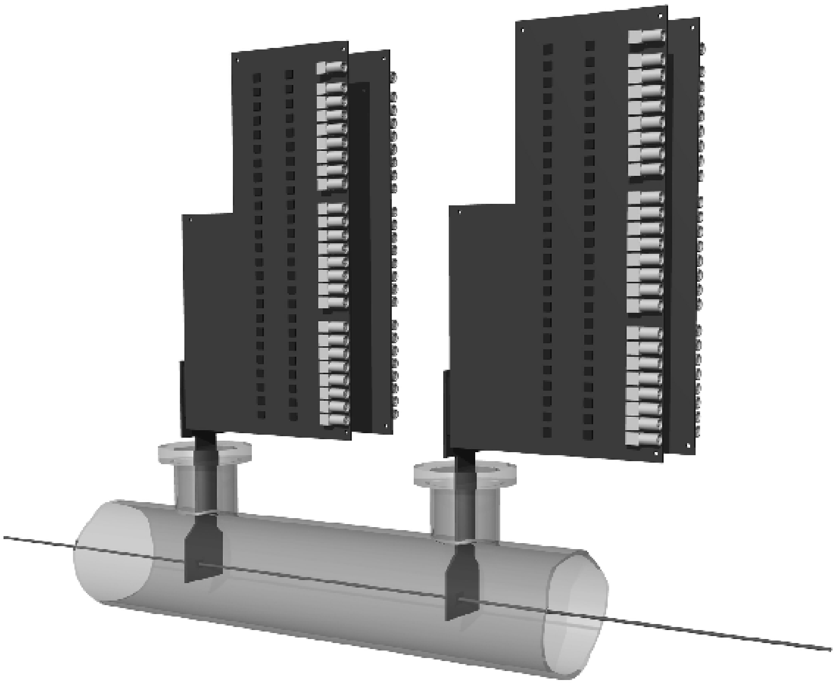

Figure 4.1: View of the Beam In silicon microstrip detectors and corresponding readout electronics. The beam comes from the right side.

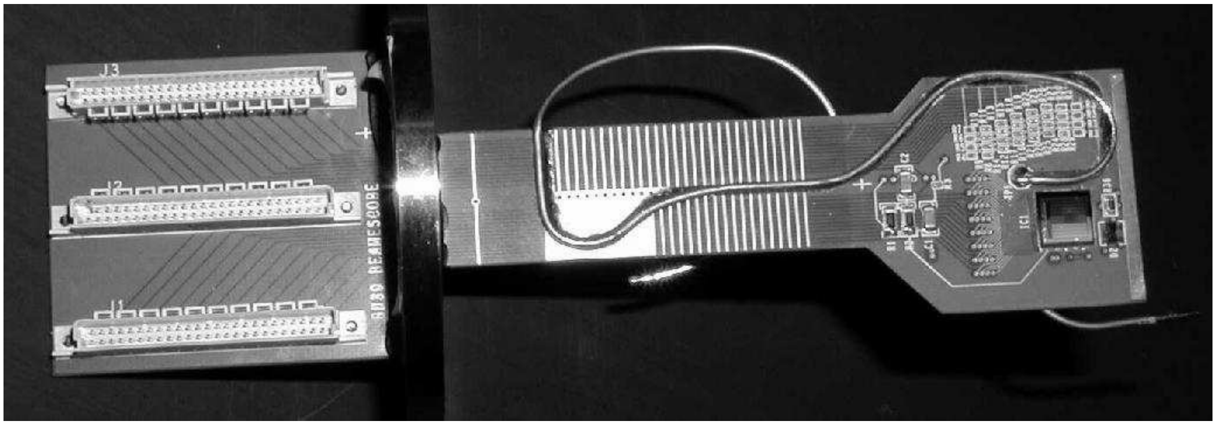

Figure 4.2: Photograph of the beamscope detector module. The sensor can be seen on the right side, placed on a hole of the PCB.

A thin-wall capillary pipe of 1.2 mm outer diameter made of cupronickel (70 % Cu, 30 % Ni) is soldered along the PCB. The pipe is fed from the transfer line and its outlet is connected to a flow meter and a manual control valve. By controlling the nitrogen flow rate in the pipe, it is possible to adjust the temperature of the detector.

Figure 4.3 shows the schematic of the Beam In readout and slow control architecture. The wide detector strips are connected to current-to-frequency converters located outside the vacuum tube. The output of these converters is connected to CAMAC scalers, which are read once per burst. The number of counts is proportional to the integrated number of Pb ions passing through the strips in the burst. This information gives an on-line beam profile on a wider area than from the small strips alone, which is used for beam steering. This readout architecture is

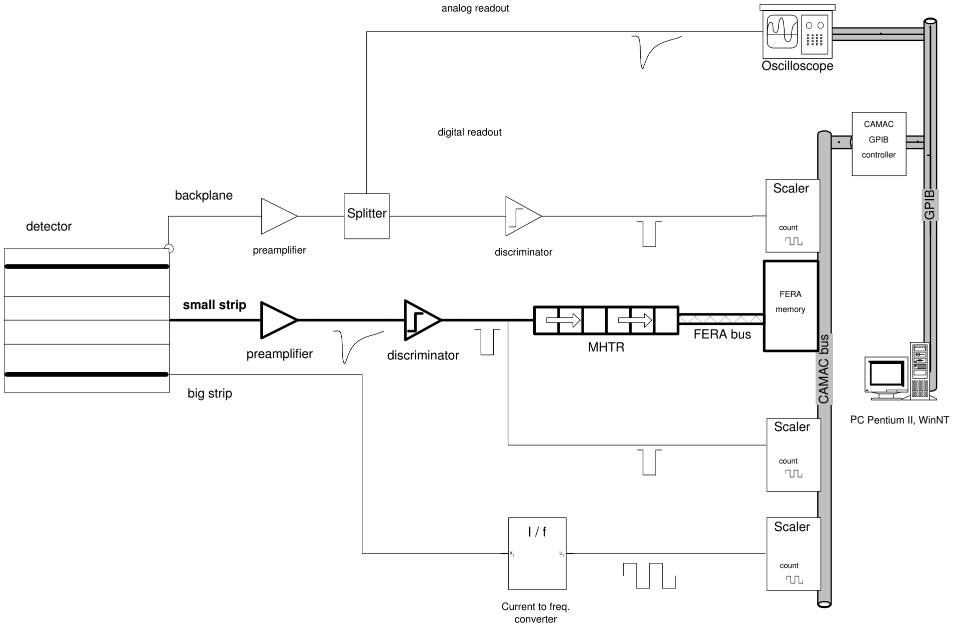

Figure 4.3: Beam In readout and slow control architecture.

simpler and cheaper than the one used for the tracking channels, described below.

The narrow strips are connected to fast voltage amplifiers placed on printed boards, which are attached to the vacuum tube. The output of the amplifiers is then connected to CAMAC discriminators (with programmable threshold). The digitized hits are then stored into a “multi-hit time recorder” system (MHTR) for 3.4 μs, which corresponds to the maximum acceptable latency time of the trigger.

The MHTR system consists of 96 “time recorder” channels (as CAMAC modules), and uses a CAMAC memory module for buffering the data of an entire burst. The time needed for encoding the data and for transferring it into the memory module is typically around 30 μs per event. The operation of the MHTR is based on digital sampling of the discriminator signals. The actual sampling clock is 150 MHz, but an interleaved sampling technique is implemented, which increases the effective sampling rate to 600 Ms/s, i.e. to one sample every 1.67 ns. The result of this sampling is transferred to a circular buffer (2 kBytes per channel) where the raw data are stored. The trigger signal is treated in the same way as the hits, so that its arrival time is determined with the same digital resolution of 1.67 ns.

The Beam Out detector is a silicon diode with a sensitive area of around 2×2 mm^2. The analog signal registered on its backplane is used to reject events with no interaction in the target. The backplane signals are used for measuring the charge deposited in the 4 BI and in the BO detectors, by means of charge integrating ADCs. However, the signals must be delayed by the trigger latency time (~ 1 μs), while maintaining their narrow shape for avoiding pile-up. This can be achieved by using optical mono-mode fibres, instead of the usual copper delay cables.

The electrical backplane signals are transformed into optical signals by modulating the current of a laser diode, and reconverted into electrical signals at the end of the fibre by means of a linear optical receiver. Such a system was already developed by the Bern group for the NA52 experiment. It was used for transmitting fast analog signals from the target area to the counting room through 350 m of optical mono-mode fibres. The original fast shape of the pulses is not degraded by this system with a bandwidth of about 200 MHz. The nonlinearity of these optical analog links is less than 2%, and the dynamic range is typically 1000.

For this experiment, five NA52-like optical links are required, one per backplane, the length of the optical fibres being defined by the exact trigger latency (about 200 m for a latency of 1 μs).

4.2 The pixel vertex spectrometer

The vertex magnetic spectrometer consists of 10 planes of silicon pixel detectors placed inside a dipole magnet (named TC8). Its purpose is the measurement of the trajectories and momenta of the charged particles before they enter the hadron absorber.

The horizontal field has an average intensity of 1.67 T over 30 cm along the beam axis. The horizontal gap of the magnet is 8 cm wide. Also the target, the BO detector and the first part of the Al_2O_3 section of the hadron absorber are placed inside the magnet. The layout of the telescope is depicted in Fig. 4.4. It starts with six planes composed by four single-chip detectors arranged in a diaphragm geometry. The remaining four planes consist of 8 bi-chip units arranged in such a way that the angular acceptance of the muon spectrometer is properly covered. The total number of chips is 88, corresponding to 721 000 channels.

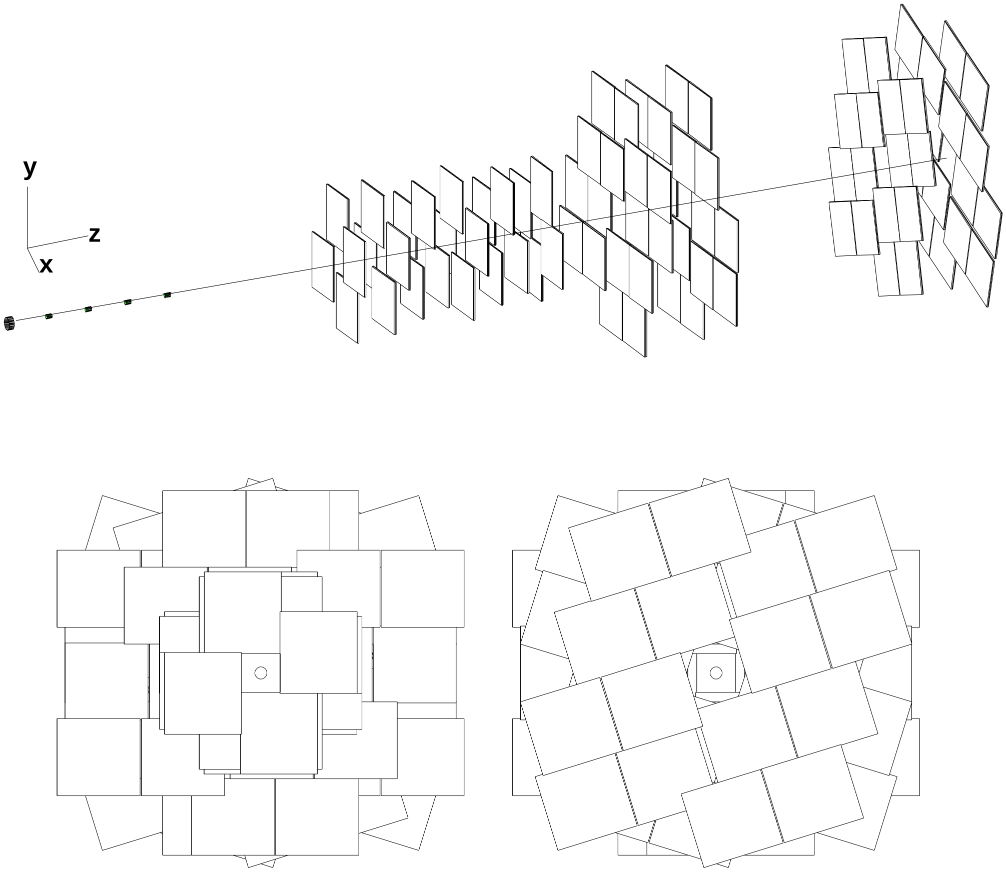

Figure 4.4: Global view of the silicon pixel telescope (top). The front view (left) and the back view (right) of the telescope are also shown.

The orientation of the pixel planes has been optimized to achieve optimum angular resolution, and to ensure good accuracy in the measurement of both transverse coordinates of the impact parameter of the muon tracks. We name Y planes (X planes) those which have the rectangular pixels oriented in such a way as to measure the y (x) coordinate with highest accuracy. The last two planes (U and V) are rotated by a ±300 mrad azimuthal angle.

4.2.1 The silicon pixel telescope

The pixel telescope is based on the Alice1 pixel readout chip, developed in the framework of the ALICE and LHCB experiments. This chip is a matrix of 256×32 pixels with binary readout. The cell size is 50×425 μm^2, the total sensitive area being 12.8×13.6 mm^2. A comprehensive description of the chip can be found in the ALICE ITS TDR [2].

In spite of having been optimized for other applications, the Alice1 chip fulfills our requirements in term of granularity, position and time resolution, and radiation tolerance. In particular, its high granularity ensures good two-track resolution, which allows tracking all particles produced up to the most central Pb-Pb collisions (at the SPS).

The Alice1 readout circuit has been designed in a 0.25 μm CMOS commercial technology for several reasons. The most obvious one is the density of functions that can be achieved with the reduced dimensions of transistors and connecting lines. The density can also be increased by using the 6 metal interconnect layers that are offered in the technology. In addition, these metal layers help in reducing cross-talk and shielding, as well as in stabilizing the power supply potentials over the fairly large chip area. By using the enclosed transistor layout and judicious placement of guard rings, it has already been shown in a previous prototype [3] that changes induced by radiation can be minimal even up to a level of several 10^{14} particles/cm^2.

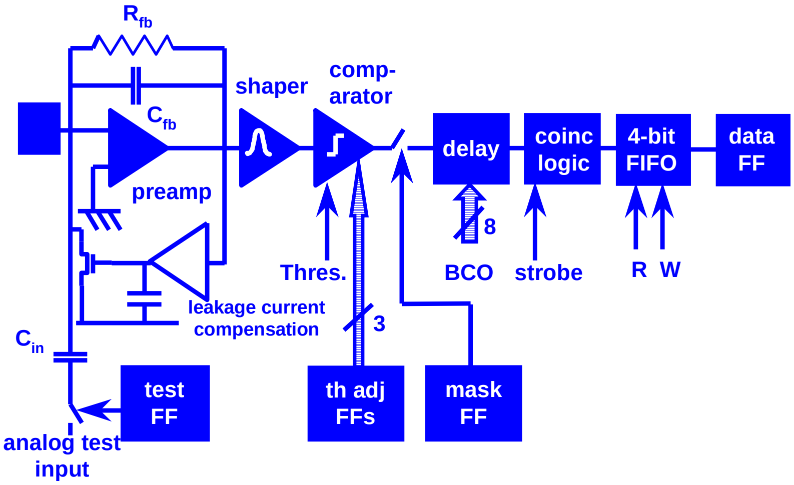

Figure 4.5: Schematic diagram of the Alice1 pixel cell.

Each front-end cell comprises a preamplifier, a shaper filter, a discriminator, a delay line, and readout logic (see Fig. 4.5). The amplifier is connected to the sensor element with a differential input configuration. While this leads in theory to an increase of noise in comparison with the single-ended connection, there is a practical improvement in performance because various forms of coherent fluctuations can be eliminated. In particular, it has been established by previous experience that the minimum possible discriminator threshold in each pixel is much more determined by disturbances transmitted via the substrate, than by the inherent noise of the amplifier-comparator system. The peaking time is 25 ns and it takes less than 200 ns for the pulse to return to zero. The input of the pre-amplifier is always connected to an injection capacitance, used for calibrating and testing every cell. In fact, the testing and qualification of the components is a key element in the production of the pixel detectors.

The discriminator threshold can be adjusted individually thanks to a 3-bits register stored locally in each cell. If a significantly lower threshold is feasible (e.g. below 2000 e^- instead of the values $\sim$4000–6000 needed in earlier experiments) this helps to increase the margin of operation under harsh conditions. A decrease of the effective collection thickness by 50 % after irradiation, should not degrade the efficiency of the detector system. Moreover, a thinner sensitive layer of the silicon sensor can be accepted. The output is connected to a synchronisation circuit, which produces a pulse with half a clock cycle duration, which goes to the delay line. A masking flip-flop allows suppression of noisy cells.

The front-end circuit has the capability to "digest" a certain amount of leakage current at its input, by active compensation built into the feedback. This part of the circuit takes into account the actual average value of current at the input of the pixel and compensates for this with a reaction time constant. Currents up to 15 nA per pixel can be compensated fully by the circuit, and this range can be extended to 100 nA if some settings are adapted. The compensation is individual in each pixel. This feature is essential to cope with the extremely inhomogeneous irradiation present in fixed target experiments.

The cell delay circuitry consists of two registers. A counter at the bottom of the chip counts continuously to N and then down to zero again. N is set such that $2\times$N is the number of clock cycles corresponding to the trigger latency time (if the required delay does not correspond to an even number of clock cycles, the strobe must be delayed by one extra cycle before being sent to the chip). When a pixel is hit, the short pulse at the discriminator output latches the counter value in both delay registers. This value is then compared with the counter content at each clock cycle. Each register has its own logic, which identifies the second true comparison and produces a coincidence pulse at the end of the delay line. The use of two registers allows delaying up to two hits in the same pixel during the trigger latency time. If a pixel has a hit in coincidence with the strobe, a logic one is latched in a 4-bit FIFO, so that up to four hits can be stored before being read out.

For setting and monitoring of the detector parameters, a powerful architecture for tests and controls based on the JTAG protocol [4] has been implemented in the Alice1 chip. The control software takes care of storing and retrieving via the JTAG bus the information about the status of the pixel registers (test, mask, 3-bit threshold setting), and of the general chip register (DAC, reference voltages, control bits, global threshold and delay). The serial JTAG bus on the chip daisy-chains all the pixels, so that registers are loaded sequentially, using column-wise addressing.

Two basic detector units will be produced. In the "single-chip" assembly, a 1.392 mm long, 1.472 mm wide silicon sensor is bump-bonded to one pixel readout chip. We also make use of "bi-chip" detectors, where a 1.392×2.872 mm^2 sensor is connected to two readout arrays. In the latter, the sensing cells in the stitched region between the two chips are 625 μm wide to ensure hermetic detection area. Since multiple scattering is an issue, in particular for vertexing capability, we will use sensors "thinned" to 200 μm.

Each logical plane of the pixel telescope is actually composed by two "arrays" or "half-planes" mechanically mounted together (with $\sim$ 100 μm precision) face to face. A small overlap between the active regions of the detectors on the two arrays allows fine alignment by tracking (better than 5 μm precision in the smaller pixel size, and better than 20 μm in the larger pixel size).

The pixel chips are glued on standard 300 μm thick ceramic (Al_2O_3) supports, which also provide the readout and control bus lines to which the chips are connected by ultrasonic wire-bonding. The multi-layer ceramic bus is mounted on a common support together with a flexible kapton cable, which ends in a standard connector. The electrical connection between the ceramic and the kapton is also achieved by wire-bonding.

The ceramic bus underneath the detectors of the first 6 planes is cut in order to reduce the material thickness traversed by the particles, and thus reducing multiple scattering. A small region around the chip edges is actually glued to the ceramic, ensuring electrical connection. Furthermore, the support is shaped in such a way that no extra material is present in our fiducial geometrical acceptance. This makes the total thickness of a single plane correspond to $\sim 0.7\%$ of X_0, for the first planes and about 2.4% of X_0 for the others.

Assuming a beam intensity of 5×10^7 Pb ions per burst, a target thickness of $\sim 15\,\%\ \lambda_{\rm int}$ and a running efficiency of 80 %, the most exposed pixel cells (located closest to the beam line) are expected to collect around 1 Mrad per week. Based on the results from previous irradiation tests, we assume that the only contribution to the dose is from secondaries and delta rays generated in the target. It is worth reminding that in this case the difference in dose accumulated in the sensor and in the readout circuitry is only of the order of 1.5 %. Given the results obtained with the prototype pixel chip (see previous chapter), we do not anticipate any problems from radiation damage in the readout electronics.

The expected leakage (generation-recombination) current in a 200 μm thick sensor, in the most irradiated area and after one month of running at 20 °C, is 120 μA/cm^2, according to the data of the RD48 collaboration [5]. This is well within the range that the electronics can handle (up to nearly 500 μA/cm^2). Moreover, since the leakage current compensation is individual for each pixel, the chip performs well also with the very inhomogeneous expected dose.

Sometimes there is excess sensor current due to edge effects or local crystal dislocations. These currents should not really influence the input of a pixel, however they may cause problems in operating the detector at the desired bias voltage. For example, the power dissipation in a sensor operated at 100 V will be around 100 mW, if currents as high as 1 mA are present.

It has been indicated above that in a pixel detector there is a large built-in margin for signal reduction, due to the very comfortable signal-to-noise margin in the beginning. A loss of signal even in excess of 50 % can be tolerated. In addition, the use of relatively thin (200 μm or less) silicon sensors eases the inefficiency in charge collection because there will be less charge trapping and a higher field can be applied with a moderate external voltage. Up to a dose of 10 Mrad one does not expect significant problems with the current pixel system design.

The expected power dissipation in each pixel is ~ 50 μW under static conditions. The dynamic dissipation depends on the actual occupancy, and is probably 20 % higher. With 60 μW per pixel the dissipation is close to 300 mW per cm^2 or 500 mW per chip, which corresponds to about 50 W for the full telescope. The power dissipation in the sensor contributes at most with an additional 10 %. The generated heat has to be evacuated, but a favorable ΔT may be assumed because the operating temperature of the pixel system in principle can be around 20 °C. The need for cooling to lower temperature, e.g. 10 °C or -10 °C may arise in case of some unexpected degradation of the sensors. The adoption of a flexible cooling scheme provides a security margin in case of any such unexpected phenomenon.

The baseline solution is to adopt gas cooling. The pixel telescope will be mounted in an insulating box inside the magnet. The box is made of an open-cell isolating foam of appropriate thickness. The gas flow coming from below the telescope is forced to go in between the pixel arrays, in order to cool the detectors in a more efficient way. We will also optimise the design of the ceramic bus, as we do for the beamscope, in order to improve the cooling scheme. The box will have small apertures at the top in correspondence of the kapton cables. The choice of the coolant has not been finalized, but this system allows us to easily choose between dry air and CO_2. Tests will be performed soon.

4.2.2 Readout electronics

The readout system for the pixel telescope is based on a VME board [6] hereafter named the “pilot board”. This board has been originally designed and produced for testing the Alice1 pixel chip. In order to use the pilot board for the readout of our silicon pixel telescope, we have introduced slight modifications to implement the VME block transfer data (BLT) mode.

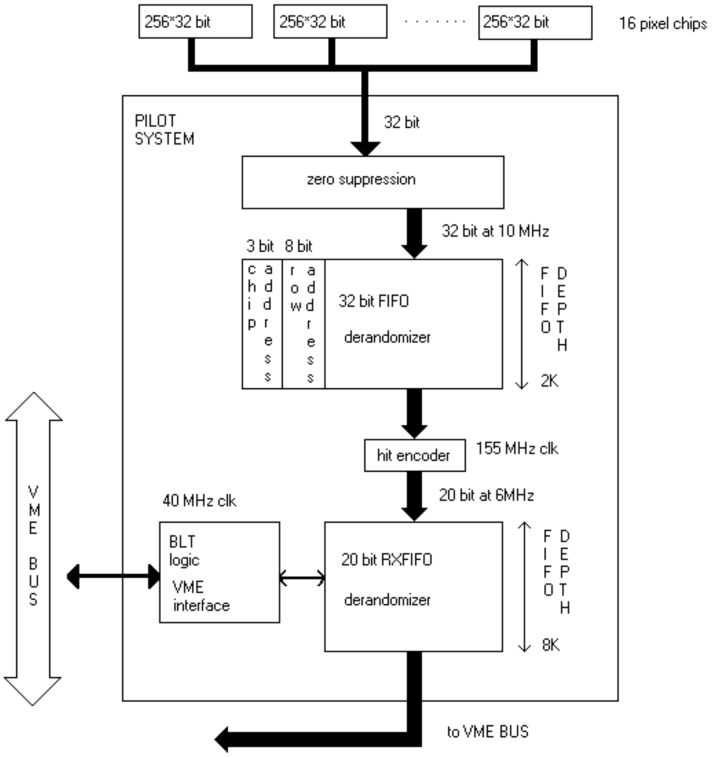

Figure 4.6: The pilot system.

The pilot board is schematically shown in Fig. 4.6. Its relevant features can be summarized as follows.

1. The pixel data are read out at 10 MHz and stored in a 2 kByte FIFO. Each card can read sequentially up to 16 Alice1 chips in series, for a total readout time of $16 \times 256 \times 100$ ns, or 409 μs. Only 32-bit words corresponding to rows with at least one hit are stored in the FIFO.

2. The data from the 2 kByte FIFO are coded into 20-bit words, one per hit, and transferred at 6 MHz into a second 8 kByte RXFIFO.

3. Data are then extracted from the RXFIFO and sent to the VME master, according to the VME BLT protocol.

In order to optimise the data acquisition system (see also Section 4.6), three pilot cards will read the data of the six small planes (24 chips in total), while four other cards will read the large (16-chip) planes. The boards will be installed in two separate VME crates, so that the burst data is read in parallel by two processors.

According to our Monte Carlo simulations, the average number of pixels hit is around 4000 for the 10 planes, and around 400 per plane. Our simulations of the readout system show that this implies that the data can be transmitted to the VME master almost at the same rate as they are read from the pixel chips: the service time to read a full event remains close to 409 μs (16 pixel chips times 256 rows at 10 MHz). This is due to the fact that reading the 2 kByte FIFO at 6 MHz does not cause queueing inside the pilot board.

Data cannot be sent continuously by BLT as they are written into the RXFIFO, because time-out errors could be generated if the time separation between two consecutive pixel words is greater than ~ 1 μs. The solution is to download the first event fully into the RXFIFO and to start a BLT only afterwards, at 5 MHz. During the BLT of the first event, the second event is downloaded into the RXFIFO and so on.

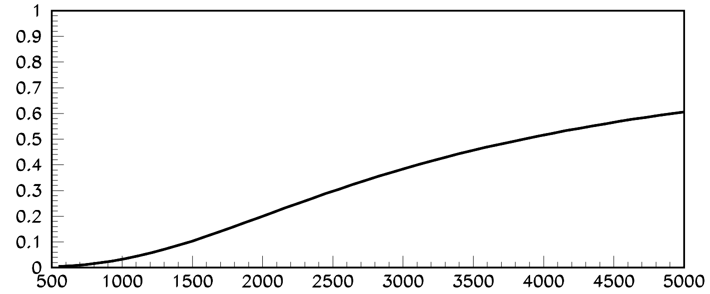

dead time vs trigger rate (Hz)

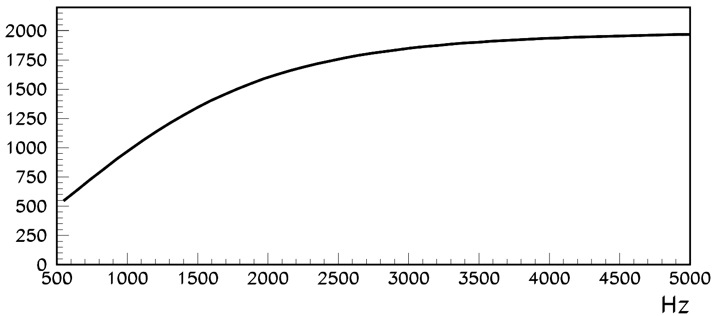

recorded events/s vs trigger rate (Hz)

Figure 4.7: Dead time (top) and number of events recorded per second (bottom) as a function of the trigger rate.

Given a certain (average) rate of events produced per second, the question of how many of them can be collected can be solved by queue theory. We assume that the events arrive in time according to a Poisson distribution. We have a queue of 4 buffers in the front end and we evaluated above that the service time about 400 μs. We conservatively increase that time at 500 μs. The system will produce dead time when all 4 buffers (the queue) are full. Figure 4.7 shows how the dead time and the number of events recorded per second depend on the trigger rate. We can see that the system is able to cope with a trigger rate of around 1500 triggers per second (more than 7000 triggers per 4.8 s burst) without any problem.

4.3 The zero degree calorimeter

The ZDC, inherited from the NA50 experiment, has already operated successfully in the 1995, 1996, and 1998 data taking periods [7]. It is a quartz-fiber spaghetti calorimeter that exploits the Cherenkov light produced by the shower particles in silica optical fibers [8]. The structure of the detector is shown in Fig. 4.8. In order to minimise the background due to participant nucleons and produced pions, a 60 cm long copper collimator was placed in front of the calorimeter. The design of the collimator was optimized on the basis of simulations done with the VENUS event generator [9]. It consists of a cylinder with an outer diameter of 60 mm and a conical aperture of 3.3 mrad, corresponding to a 7 mm radius hole on the ZDC front face. The pseudo-rapidity region covered by the detector is $\eta \geq 6.3$.

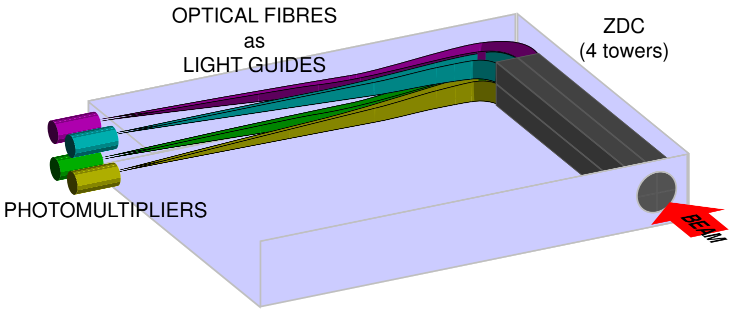

Figure 4.8: Mechanical structure of the ZDC.

The ZDC consists of 30 grooved tantalum slabs (1.5 mm thick), stacked to form a parallelepiped of $5 \times 5 \times 65$ cm^3. The active part of the detector is made of 900 quartz fibres, uniformly distributed with a pitch of 1.5 mm, corresponding to a quartz to tantalum volume ratio of 1/17. The fibres are of HCG-M-365-U type, and have a 365 μm diameter pure silica core and 0.22 numerical aperture. The total length of each fibre is 180 cm. The first 65 cm, embedded in tantalum, represent the active part of the calorimeter. The rest (bent at 90° with respect to the beam axis) act as a light guide towards the photomultiplier tubes (PMTs) located about 1 m from the beam axis, to reduce background caused by shower particles impinging on the PMT windows. In order to be position sensitive, the ZDC is divided into four towers, each one grouping 225 fibres, and being read out by one photomultiplier. The coordinates of each Pb ion entering the ZDC can be determined by evaluating the centroid of the shower.

Around 60% of the hadronic shower generated by a proton of 158 GeV entering the centre of the ZDC is contained in the detector. The fluctuations in this fraction dominate the resolution of the detector. Statistical fluctuations on the number of photoelectrons are negligible, since the observed light yield is around 0.5 photoelectrons per GeV.

The ZDC is equipped with four 6-stages photomultipliers (Philips XP2242-B), operated at a gain of about 5×10^3, corresponding to a mean anode current of 30 mA when the detector is exposed to the full intensity lead beam (5×10^7 Pb ions per burst). The signals are sent to the counting room through $\sim$200 m long cables. To preserve the excellent time quality of the Cherenkov signals, bridge-T filters were used before the last stage of amplification. The signal width allows a gate of 12 ns to be used, compatible with the high-intensity beam required by the experiment.

Even in the most central collisions a residual energy of 2–3 TeV is emitted at zero-degree. With a dynamic range of about 10 (from 3 to 33 TeV), the ZDC signal can be discriminated to provide the “minimum bias” trigger.

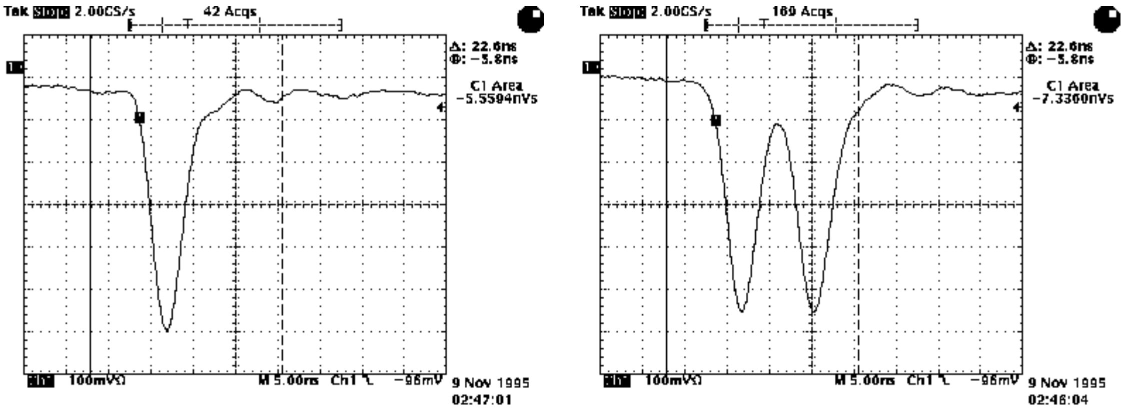

Figure 4.9: Signal of one PMT of the ZDC in case of a single incident Pb ion (left) and when two ions follow each other (right) by a few ns. Notice that the grid has 5 ns steps.

The ZDC has to cope with counting rates around 10^7 Pb ions per second. In spite of the short duration of the signals and of the ADC gate (about 10 ns), this rate causes pile-up effects, that can introduce a bias in the measurement of the centrality. Therefore, special care has been taken to identify and reject pile-up events. We have developed a method for pile-up identification that only uses ZDC information. The basic idea is that when the time interval between the arrival of the two ions is smaller than ~ 10 ns, the two are superimposed, leading to a signal shape different from the standard one. This can be seen in Fig. 4.9, which shows the ZDC signals due to a single ion (a) and to two superimposed ions (b). The shape of the analog sum of the signals from the four towers was analysed by 24 ADC channels with each (12 ns wide) gate delayed by 2 ns with respect to the previous one. Pile-up events are identified by comparing the pattern of the 24 ADC channels, for each event, with a reference pattern corresponding to standard signals with no pile-up. The pile-up recognition efficiency obtained with this method is around 97 %.

The resolution of E_{ZDC} obtained at the beginning of the run was 6%. During data-taking, the ZDC was continuously monitored by checking the position of the “Pb peak”. The stability of the response of the photomultipliers was monitored by means of a laser diode pulse light optically connected to each photomultiplier through a quartz fibre.

In Fig. 4.10 the position of the Pb peak is shown as a function of the integrated radiation dose D_{max} absorbed by the detector throughout the NA50 1996 and 1998 data taking periods. Clearly, the signals decrease with the dose, but can be recovered by simply increasing the gain of the PMTs.

The dose D_{max} has been evaluated by means of a Monte Carlo simulation based on the GEANT code. It represents the dose deposited in the four fibres closest to the axis of the ZDC, at a depth corresponding to the maximum development of the shower (i.e. between 1 and 2 λ_{int}).

In Fig. 4.11 we can see how the resolution deteriorates as a function of the dose received during the same data taking period. After an initial worsening from 6 to 8%, the resolution remains stable.

4.4 The muon spectrometer

The muon tracks will be measured by the muon spectrometer originally built for the NA10 experiment [10] and which has been used by the NA38 (years 1986–1992) and NA50 (years

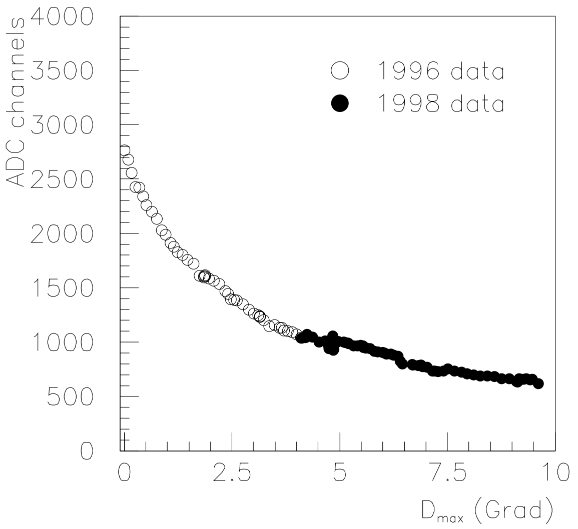

Figure 4.10: Position of the lead peak in the ZDC spectrum as a function of the dose $D_{\max}$ absorbed by the detector throughout the 1996 and 1998 NA50 data-taking periods.

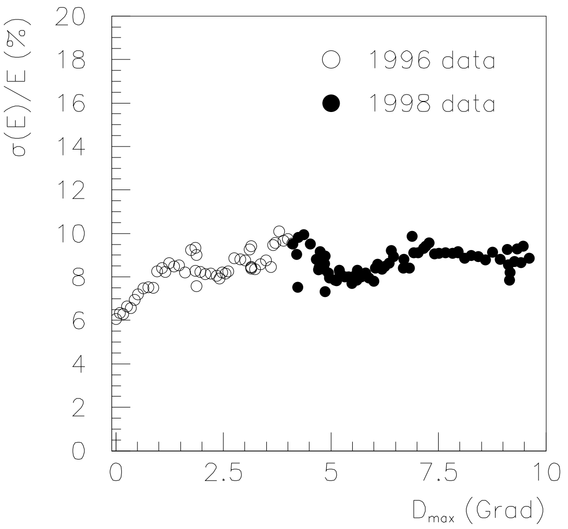

Figure 4.11: Resolution $\sigma(E)/E$ on the ZDC peak measurement as a function of the dose absorbed by the detector throughout the 1996 and 1998 NA50 data-taking periods.

1994–2000) experiments.

The muon spectrometer is illustrated in Fig 4.12. It starts with the hadron absorber, followed by four multiwire proportional chambers and two hodoscopes (R1, R2) of plastic scintillator slabs (of 2 ns time resolution) used to create the trigger. A second set of chambers and hodoscopes is placed after the air-core toroidal magnet (ACM) of hexagonal symmetry, the last hodoscope (R4) being protected by an iron wall.

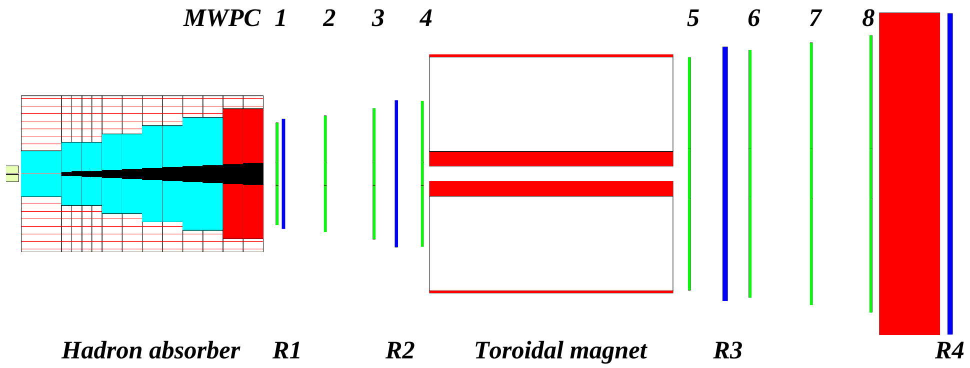

Figure 4.12: Overview of the muon spectrometer: muon filter, chambers (MWPC), trigger hodoscopes (R), magnet, iron wall. The small box on the far left represents the "pre-absorber".

4.4.1 Hadron absorbers

In its standard configuration, the muon filter is composed of ~ 50 cm of Al_2O_3 (the "pre-absorber") followed by 480 cm of carbon (corresponding to 22 X_0 and 11 λ_{int}, or 15 pion absorption lengths, enough to stop the hadronic showers), completely covering the angular acceptance of the spectrometer ($\sim$35 to $\sim$120 mrad). The muon filter materials are chosen among low atomic number elements so that the muon trajectories are not too much affected by the (Coulomb) multiple scattering. Therefore, some energetic hadrons can ‘punch-through’ the graphite blocks and cross the trigger hodoscopes. To prevent fake triggers, the last hodoscope, R4, is placed behind a 1.2 meter thick iron wall that absorbs the remaining hadrons. This wall, placed after all the MWPCs, has no effect on the dimuon mass resolution.

4.4.2 ACM magnet

The main component of the muon spectrometer is the air-core analyzing magnet (ACM). The toroidal field is produced between 6 radial iron poles, 4 m long, covering 18° in azimuth. The magnet acceptance is confined between an inner radius of 29.5 cm and an outer radius of 154 cm, values that determine the angular acceptance (and thus the rapidity window) of the whole experiment. The magnet is centered 11.3 m downstream from the center of the target. The central hole between the coils has a radius of 9.5 cm. To improve the mass resolution, the events (30 %) where one of the muons goes through one of these iron sectors are rejected from the final analysis event sample. To optimise the acceptance for low mass dimuons, we will run the magnet with a current of 3000 A, while the studies of open charm and charmonia production will be made with 7000 A. The current is pulsed, syncronized with the SPS cycle. The toroidal field is essentially azimuthal and $1/r$ dependent, $\vec{B}(r) = B_0\,/\,r \cdot \vec{e}_\phi$, with $B_0 = 0.16$ T m (0.38 T m) for $I = 3000$ A (7000 A).

In this kind of field, and with the magnet axis aligned with the beam line, a particle emitted from the target remains in the same azimuthal plane. The trigger logic, explained below, is based on this property. The deflection (polar) angle is, to a very good approximation, inversely proportional to the particle’s transverse momentum.

To prevent any systematic effects related to the field signal, the polarity is reversed every few runs. The magnitude of the field is continuously measured by a Hall-effect probe, with a $\sim$ 0.2 % precision, while the current is monitored using a precision shunt sensitive to $\sim$ 0.1 % current variations. The measured field map has been parameterized analytically by polynomial and spline functions to be used in the off-line simulation and reconstruction programs.

4.4.3 Detectors

The muon spectrometer detectors, trigger hodoscopes (R) and multi-wire proportional chambers (MWPC), all of hexagonal symmetry, are listed in Table 4.1.

The four R hodoscopes are used to trigger the data aquisition system. The first two, located upstream of the magnet, have an homothetic geometry pointing to the target region. The 30 scintillator slabs of each sextant, disposed parallel to the outer border, have a width that increases radially, from the most central one, in a geometrical progression. The R1 slabs slightly overlap each other. This way, the slabs of R1 and R2 that are hit by a particle emitted from the target, with any production angle, have always the same sequential index, i (with $i = 1,\ldots,30$). A coincidence $R_1^i \times R_2^i$ ensures that only such configurations can give a trigger. In order to account for the spatial extension of the target system and to allow for some multiple scattering of the low energy muons, the coincidence $R_1^i \times R_2^{i-1}$ is also accepted.

There is only one photomultiplier per slab of the R hodoscopes and the propagation time of the light varies with the crossing point of the muon along the slab. To eliminate such time

Label	z (cm)	Main characteristics
MWPC 1	547	y, u, v planes; 448 wires per plane; $\varnothing = 134$ cm
R 1	560	6 × 30 scintillator slabs of 1.05–3.55 cm width
MWPC 2	643	y, u, v planes; 512 wires per plane; $\varnothing = 153$ cm
MWPC 3	740	y, u, v planes; 572 wires per plane; $\varnothing = 172$ cm
R 2	784	6 × 30 scintillator slabs of 1.25–3.85 cm width
MWPC 4	835	y, u, v planes; 640 wires per plane; $\varnothing = 192$ cm
Magnet	850–1333	
MWPC 5	1365	y, u, v planes; 1024 wires per plane; $\varnothing = 306$ cm
R 3	1436	6 × 24 scintillator slabs of 5.5 cm width
MWPC 6	1486	y, u, v planes; 1088 wires per plane; $\varnothing = 326$ cm
MWPC 7	1607	y, u, v planes; 1152 wires per plane; $\varnothing = 345$ cm
MWPC 8	1725	y, u, v planes; 1216 wires per plane; $\varnothing = 364$ cm
Iron wall	1742–1862	
R 4	1882	6 × 32 scintillator slabs of 5.5 cm width

Table 4.1: Detector components of the muon spectrometer. The z scale, inherited from NA10, starts 45 cm downstream of the target center.

fluctuations (jitter) in the trigger, the corresponding slabs in R1 and R2 have their PMs at opposite ends and their signals are injected in mean timers, giving a coincidence trigger with a very small jitter ($\sim$ 3 ns). All the slabs of the R3 and R4 hodoscopes have the same width (5.5 cm). Figure 4.13 illustrates the information provided by the R hodoscopes, displaying a typical dimuon event collected with a proton beam.

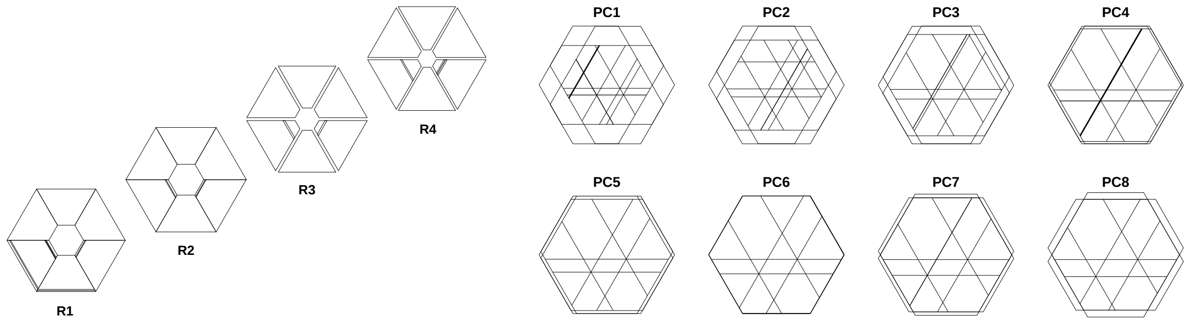

Figure 4.13: Hodoscopes (left) and chambers (right) information in a typical event. The slab combination which gave the trigger is easily recognized.

The 8 MWPCs have 3 independent (anode) wire planes, inter-spaced by 2.2 cm, with a 60° relative rotation, each of them protected by 2 graphited mylar (cathode) planes. All these 24 wire planes have 20 μm gold-plated tungsten wires of 3 mm inter-spacing. The 4 chambers upstream (downstream) of the magnet have 749 (1229) wires per plane, but only those in the acceptance region are equipped with pre-amplifiers (see Table 4.1). The gas mixture used in the chambers contains argon (80 %), isobutane (19.8 %) and freon (0.2 %), being continuously monitored from the counting room. Figure 4.13 illustrates the chambers operation.

Every new period of data taking starts with a special "alignment run", using a *single muon* trigger, a low intensity beam and no magnetic field. The off-line track reconstruction of these events imposes adjustments in the set of parameters defining the chambers' geometry, so that perfect straight lines are obtained. Typical displacements from one year to the next are of the order of 100 μm.

4.4.4 Acceptance

The main parameters which determine the acceptance window of the muon spectrometer are the angular aperture of the magnet, $35 < \theta < 120$ m rad, the magnitude of the ACM magnetic field and the number of radiation lenghts of the hadron absorber. The dimuon acceptance depends essentially on m_T and, for a given m_T, on the difference between the azimuthal angles of both muons, $\Delta\phi$, with an 'oscillating' pattern due to the magnet hexagonal structure, with six iron poles of 18° 'dead-zone'.

4.5 Trigger

The experiment will run with two different triggers: the dimuon trigger, source of all the physics data, and the strongly down-scaled "minimum bias" trigger ($\sim$5–10 % of the dimuon trigger rate). The latter is provided by the ZDC, in the heavy-ion runs, when the analog sum of its four photomultiplier amplitudes exceeds its threshold for head-on collisions (2 TeV for Pb-Pb). The minimum bias data can be used to produce normalized positively and negatively charged hadron distributions, in the window $2.8 < \eta < 3.8$.

In order to build the dimuon trigger, the R1–R2 coincidence, which selects two muons from the target region, is combined with the R4 information to provide a rough measurement of the deflection angle (at the magnet central plane) and, therefore, of the muon's p_T. The R3 hodoscope (redundant) information is useful to eliminate accidental coincidences between two uncorrelated tracks. The 'standard' dimuon trigger logic requires that the two muons are in different sextants.

The trigger rates were estimated on the basis of NA50 trigger rates, extrapolated with some guidance from simulation, to the two configurations proposed for the "low mass" and "high mass" data. In both cases, they are compatible with the proposed DAQ system. The like-sign events will probably be downscaled, using the R1–R4 trigger information.

4.6 Data acquisition and online software

The data acquisition system will have a modular structure based on VMEbus readout and commodity PCs directly connected to VMEbus. We are currently studying several commercial VME to PCI interfaces. The PCs will have enough RAM and CPU resources to gather all the data within a full burst, format the events and ship them to a central collection point (an event builder PC), where the complete events will be assembled, filtered and temporarily stored on local disks. The data will eventually be transferred to the CERN/IT central data recording facilities (CDR) by the standard CDR daemons and removed from the local disks. The front-end PCs and the event-builder PC will be connected by a switched 100 MBit/s Ethernet network.

The data acquisition software will be developed within the DATE (Data Acquisition and Test Environment) framework [11] (see Fig. 4.14).

The resources required by the data acquisition process can be evaluated as follows. Assuming a trigger rate of $\sim$4000 triggers/burst and 20 kBytes per average Pb-Pb collision, a total of

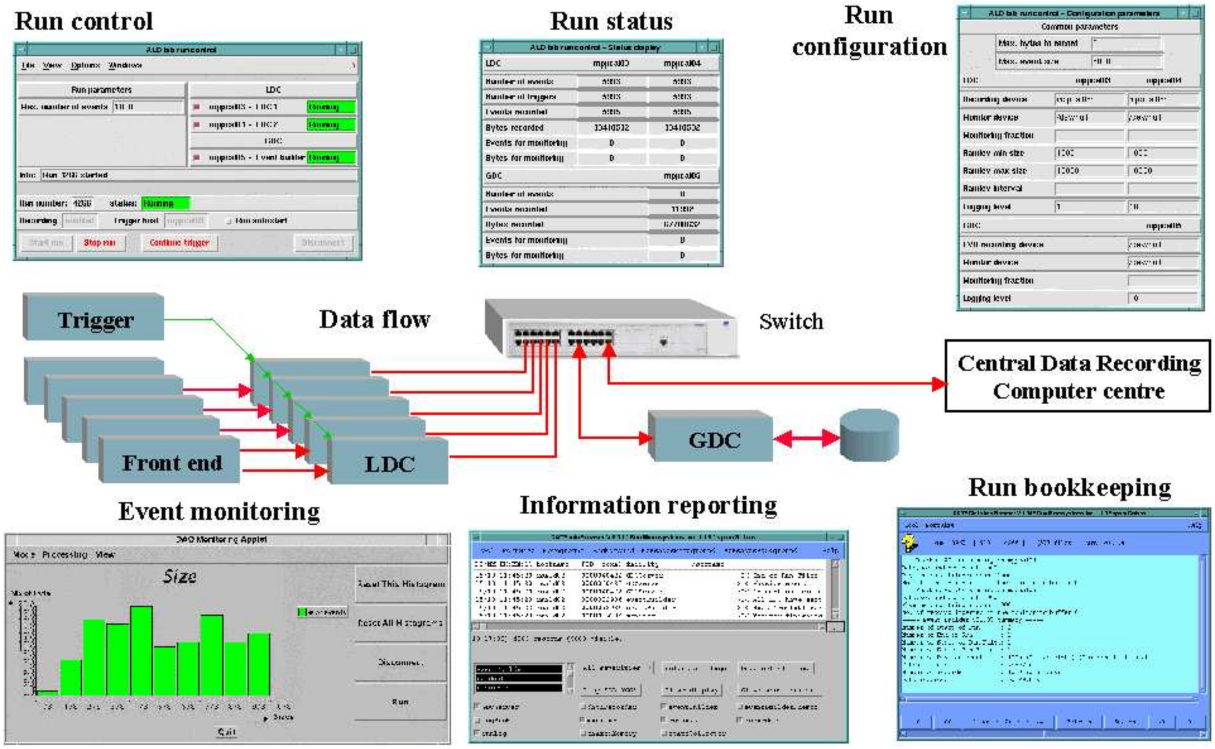

Figure 4.14: Overview of the DATE framework.

$\sim$ 80 MBytes should be collected during each burst, at an average rate of $\sim$ 20 MBytes/second. The readout process will be distributed between several CPUs, each handling a fixed slice of the data stream (a certain set of pixel planes). The number of CPUs and the partitioning of the data stream will be decided according to functional and performance requirements. An easy approach would associate each sub-detector to one CPU, but this may not be optimal as some sub-detectors (such as the pixel telescope) could give too much data (and therefore need further sub-partitioning) while other subdetectors may be grouped and handled by a common CPU (to save on resources, system management and run-time control and monitoring). Other parameters, such as VMEbus occupancy, VMEbus slot allocation and power consumption and CPU power, will be taken into account. If needed, one or more DATE “equipments” will be defined and implemented, to allow modular validation, integration and migration according to the final needs of the experience.

During the readout process, each sub-event will be tagged with a unique identification number. During the inter-spill period, the collected sub-events will be sent to a central PC where a dedicated event-building process will create the final events. According to the expected events rate, the event builder will receive data at an average rate of $\sim$ 5.5 MBytes/second. This throughput can be effectively handled by the foreseen Ethernet network. The raw output from the event builder will reach $\sim$15 GBytes/hour (corresponding to a maximum of $\sim$ 0.37 TBytes/day). The event builder will reformat and pre-process the complete events and send them to a fast filtering process, which will provide a reduction factor between 3 and 10 of the data volume.

The filter will perform the reconstruction of the tracks in the muon spectrometer at the filtering stage. Events with at least one muon crossing the magnet iron will be rejected at this stage, while low-mass pairs will be pre-scaled. Events with tracks with the same charge will also be downscaled. It is interesting to mention that the DATE system allow to set-up a DAQ scheme with more than one event-building PCs, thus providing a longer time for the filtering process and the possibility of implementing more complex algorithms. Moreover another filtering stage could possibly be arranged on the IT side to further reduce the data volume. Those two schemes have not been studied yet in details but we investigated the possibility of implementation in case of budget or off-line analysis resources limitations. While the temporary storage is performed on relatively cheap hard disks, one should try to reduce as much as possible the amount of tapes written.

The data produced by the event-building and filtering process will be stored on the event-building PC local disks. The standard CDR daemons will then copy the data to permanent media on the CERN/IT building. The choice of the suitable media is under study but the CDR already supports most of the present standards. The event-building PC will be equipped with at least two independent SCSI disks. Such a scheme will allow the event-building process and the CDR daemons to efficiently exploit the PC resources. The event-building will write on a disk while the CDR copies data from the other one, thus avoiding the slowing down of the disk access speed due to concurrent access of the same media. The disk size will determine the time during which the DAQ system can continue to take data in case of connection problems with IT. Nowadays commercial low-cost SCSI disks of up to 36 GBytes are available. This corresponds to at least 5 hours of continuous data taking (assuming a filter reduction factor of 3). The event-building PC will also be equipped with a standard *full-duplex* Ethernet interface, allowing the input (event-building) and output (CDR) processes to exploit in parallel the full 100 MBit/s Ethernet band-width. For the physical connection between the event-building PC and IT we plan to use the direct optical Gigabit Ethernet connection set up for the NA48 experiment, that has been successfully used over the past 3 years with much larger data rates ($\sim$ 260 MBytes/burst) and extremely good stability.

Additional PCs will be running monitoring tasks. They will be connected to the switched Ethernet network and will receive a programmable fraction of the data either from the front-end PCs (for local monitoring of the hardware performances) or from the event-building PC (for "physics" monitoring). This functionality is present in the DATE software.

In spite of the significant upgrade with respect to the NA50 DAQ system, the proposed data acquisition architecture is completely based on existing technologies. Therefore, we do not anticipate any problem in achieving the expected performance.

4.7 Offline software framework

The presence of a pixel telescope with 700 000 channels and the rather demanding issue of track reconstruction and matching impose a radical change in the offline framework, away from the 20-year old Fortran-Patchy-EPIO software environment of NA50. We will adopt a state-of-the-art Object-Oriented programming framework, using the ROOT package and the AliRoot environment, as developed for the ALICE experiment.

The choice of such a scheme, will improve our programming efficiency for many reasons. Object-Oriented programming allows to split the code into small independent modules (improving the efficiency of maintenance and of shared development) and to inherit from already developed code (we can reuse many general utilities and concentrate on our specific algorithms).

The Root framework has a scripting language (C++), allowing a faster development of algorithms, as it is possible to test and debug them without going through the compilation, loading and running steps. Root has also object-oriented database facilities, which allow to keep track of the evolution of the experimental setup with time. The data are written together with the version of the code needed to process them, facilitating considerably the version control.

The AliRoot environment runs on several operative systems, including Linux. It is composed of many packages, mostly independent from each other, with the exception of a set of base classes. It fully implements the inheritance mechanism of C++, allowing the base classes to handle detector responses, particle generation and transport code in a generic way. It is possible to interchange one generator with another, switch from Geant3 to Geant4 or FLUKA, for instance, and simulate only certain detectors, without interfering with the rest of the software. We intend to use the steering package of AliRoot and to implement only the code we need for our specific detectors. For instance, the tracking, hit simulation, digit clusterisation and display algorithms will be used as such. Figure 4.15 shows the result of a peripheral Pb-Pb collision, as seen through our AliRoot based simulation package.

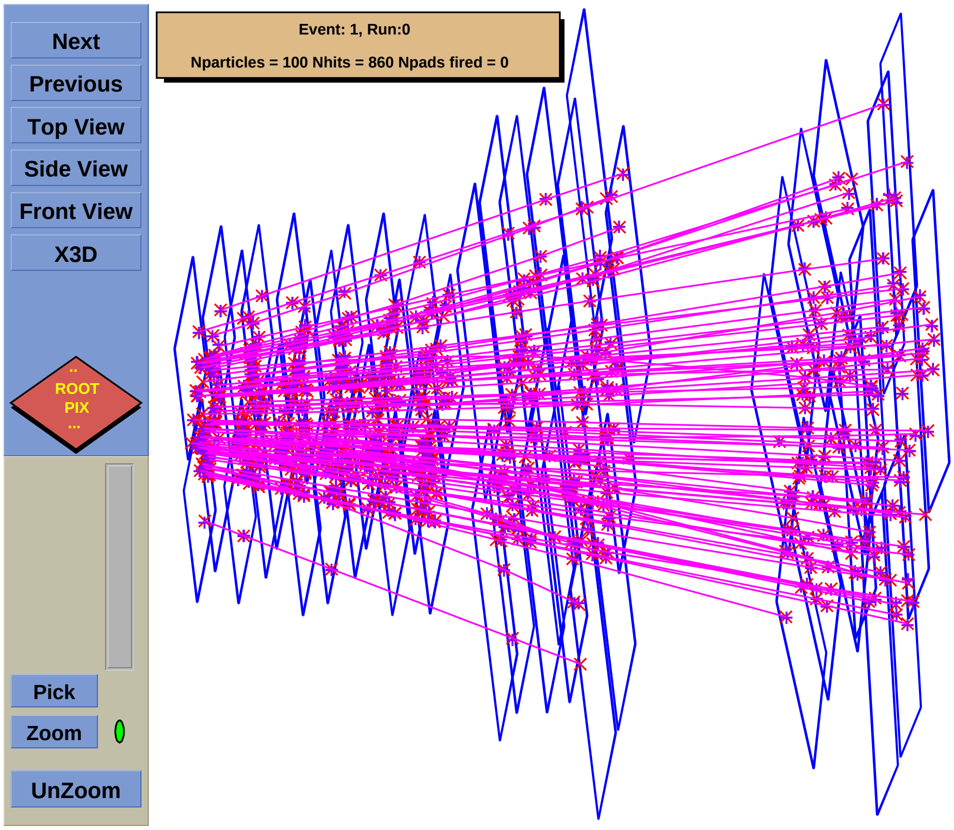

Event: 1, Run:0

Nparticles = 100 Nhits = 860 Npads fired = 0

Figure 4.15: Event display of the pixel spectrometer, made with our AliRoot based simulation software.

The expected event size for average Pb-Pb collisions is around 20 kByte. Assuming a trigger rate of 4000 events per spill we anticipate a data flow of 80 MByte per burst. With this data rate and assuming 75 % running efficiency we should collect about 2 TByte per week of Pb-Pb running, which we plan to store using CERN's central data recording system. Compared to other CERN experiments this is a minor challenge. For instance, CERES and NA49 are presently storing around 1 TByte of data *per day* while Compass expects 2–3 times more.

We will request from the CERN computing center enough storage media and CPU power to do the reconstruction of the collected data. A preliminary estimate indicates that the reconstruction of the data collected in 30 days of running can be done in less than three months using the equivalent of ~ 50 of the currently available 400 MHz "commodity" PCs.

5 Physics Performance Simulations

In this chapter we present the results of the Monte Carlo simulations performed to evaluate the physics performance capabilities of the experiment.

5.1 Criteria for choice of setup

We recall in this section the criteria used in the optimization of the experimental setup. The NA50 dimuon spectrometer is configured for maximal acceptance for soft muons. The hadron absorber (Al_2O_3 and C, except for the last 20 cm which are replaced by Fe) is as light as compatible with safe functioning of the multiwire chambers.

The open charm data will be taken with the "high mass" (HM) setup, with a current of 7000 A in the toroidal magnet. The acceptance for dimuons from open charm pairs is then the same as with the 80 cm Fe and 4000 A foreseen in the LoI [1], while the J/ψ (and ψ') acceptance and mass resolution both improve by $\sim 40\,\%$. The beam intensity will be 5×10^7 Pb ions per 4.8 s spill, every 19.2 s. We will run with up to 5 targets, of Pb or Ag, each of them 1.5 mm (Pb) or 2.0 mm (Ag).

The "low mass" (LM) configuration will be obtained by lowering the toroidal magnet current to 3000 A, for the study of the mass region from threshold up to and including the ϕ meson, adapting the beam intensity and target length to the much higher trigger cross section. In particular, our physics performance simulations assume a beam intensity of 10^7 Pb ions per spill. Since the composition of the hadron absorber remains the same, we can swap from one setup to the other in a few minutes.

The vertex spectrometer uses the dipole magnet and field already used in the 1998 tests. Its goal is to detect the trigger muons with close to 100 % efficiency, as well as all charged particles emitted in the same angular window ($3 < \eta < 4$, or $35 < \theta < 110$ mrad). The Alice1 chips have an active area 3.4 times larger than those used in our 1998 tests. We will use them bump-bonded to single chip sensors, with 4 chips arranged in fan-like topology around the beam hole (first 6 planes), and bump-bonded to bi-chip sensors, 8 of them in each of the four last planes. The layout of the pixel telescope is shown in Fig. 4.4. The first six (small) planes have orientations X,Y,Y,Y,Y,X and are positioned equally spaced (by 1.2 cm) between 7.6 and 13.6 cm downstream from the center of the target. The remaining (large) planes are positioned at 16, 18, 24 and 26 cm, the first two being Y planes and the last two being azimuthally rotated by ±300 mrad with respect to the Y position. As explained in the following lines, this layout was optimized having in mind the problems of occupancy, radiation dose, multiple scattering, pointing accuracy, redundancy, luminosity and alignment.

The innermost active pixels of the first, 4-chip, planes are at 3.2 mm from the beam axis, where the occupancy reaches 12 % for central Pb-Pb collisions. They should survive the dose of 2.7 Mrad corresponding to one month at 5×10^6 Pb-Pb interactions per burst, including secondary interactions and delta rays. If needed, these small planes can be replaced during the run. The reaction rate would then be kept such as to guarantee survival of the large 16-chip planes, which survive three times longer, their most exposed pixels being at 4.8 mm from the beam line.

Multiple scattering in the pixel planes is not a crucial factor for the measurement of the muon momenta. Indeed, the values measured by the muon spectrometer are anyway more accurate, and are used to constrain the trajectories of the muons throughout the pixel detectors, after track matching. However, the accuracy of the extrapolation of the muon tracks towards the primary vertex strongly depends on the multiple scattering in the first pixel planes. These carry only 4 chips each, wire bonded to the readout bus on the edges away from the beam. Therefore, they hang almost free in space, so that the muons traverse only 0.75 % X_0 per plane, three times less than the 2.4 % X_0 of the large planes, whose ceramic bus covers most of the active detector area. The resulting mean accuracy of the vertex extrapolation is $\sigma_{v,y} \simeq 30\ \mu$m. A similar extrapolation accuracy in x, $\sigma_{v,x} \simeq 30\ \mu$m, is achieved by inserting 2 small planes turned by 90° near the target, and by tilting azimuthally the two last large planes.

Redundancy, largely lacking in the 1998 tests due to the bump bonding crisis, has been built into the layout, which essentially requires 3 well measured space points. The last one is given by two planes, azimuthally tilted to give good y and moderately good x information, and reversed with respect to each other, so that the (small) holes of one are well covered by the other. The two large Y planes, of $\sim 100\,\%$ geometrical coverage, measure the sagitta (the track projections on the $x-z$ plane are virtually straight lines). The six smaller planes, of orientations X, Y, Y, Y, Y, X, ensure that the trajectory of the muons will be measured in x and in y, whatever the target where they are produced, and provides several space points to most muons, in this high occupancy region.

A multiple target of 1 mm diameter subtargets spaced by 12 mm in z ensures the interaction rate of a thick target, while reducing to around half a subtarget length the material traversed by the muons in the angular acceptance of the spectrometer, thereby minimizing multiple scattering. Small subtargets also suppress the $e^{\pm}$ tracks of electromagnetic showers. The first subtarget, not being crossed by particles produced upstream, can have a diameter of 3 mm, to completely intercept the beam profile.

Alignment to pixel precision will be reached with the straight lines provided by a defocused, low intensity Pb beam, in particular by those Pb ions which cross both the outer parts of the 50 μm pitch microstrips of both beamscopes and the corresponding innermost regions of the pixel detectors. These will allow to measure the position and angle of the beamscopes with respect to the pixel spectrometer, at the beginning of the run, and to monitor the alignment during the run.

5.2 Data reconstruction and event selection

To simulate the physics performance of the experiment, we generated the soft particles according to thermal distributions, while for hard processes we used the PYTHIA event generator [2], with the MRS A parametrisation [3] of the parton distribution functions. The hadronic background in the vertex spectrometer was generated with the VENUS event generator [4]. The muons and hadrons are then tracked through the experimental setup, taking into account multiple scattering, by using the detailed Moliere formulation, and energy loss.

The event reconstruction procedure can be divided in several steps, which are summarized in the following. The first step is the reconstruction of the muon tracks in the dimuon spectrometer, which is performed using a modified version of the standard NA50 reconstruction software package, taking into account the presence of the dipole field in the vertex region.

After the clusterization of the hits in the pixel planes, the reconstruction of all the tracks in the vertex spectrometer is done taking into account the information from the beamscope detector (x and y coordinates of the interaction vertex, within $\sim 20\ \mu$m precision), which allows rejecting a large fraction of spurious tracks (random combinations of hits in the pixel planes) and reduces the computing time needed for pattern recognition by a factor ~ 10.

Using the reconstructed tracks, the interaction vertex is fitted using the weighted gaussians sum method, which suppresses the "outlier" tracks (tracks which do not converge to the interaction point). Already at this stage most of the muon tracks due to π and K decays are suppressed. In fact, many of the muons coming from hadrons which decay within the vertex spectrometer correspond to tracks not pointing to the vertex and are rejected during this reconstruction step.

For the study of open charm production, where we are interested in offsetted tracks, the reconstruction includes an additional step: the clusters belonging to tracks pointing to the vertex are suppressed and the reconstruction procedure is repeated for the remaining clusters without constraining the track to converge to the vertex.

The next step is the selection, among all the tracks reconstructed in the vertex telescope, of the candidates to match the muons measured in the dimuon spectrometer. The selection is based on the comparison of the angles and momenta of the tracks, as measured in the two spectrometers. A "matching χ^2" is defined as the weighted square of the differences of the curvature (inversely proportional to the momentum) and of the slopes in the $x-z$ and $y-z$ planes. The tracks with minimum χ^2 are selected.

The matching procedure depends on whether we want to select prompt or displaced vertex (charm decays) muon tracks. In the case of the prompt dimuon analysis, the matching is done on the sample of tracks that point to the vertex. When looking for charm decays, the matching procedure is performed using the tracks which have a minimum offset from the origin.

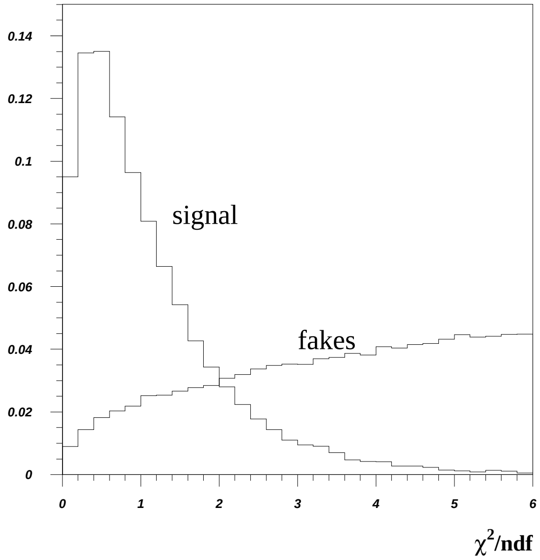

Figure 5.1: Matching χ^2 normalized distribution for the true and fake matches.

Together with the real muons, we may also have among the candidate tracks a certain number of hadrons, causing fake matches. This happens when the near by hadrons match the selection criteria as well or better than the real muon track. Figure 5.1 shows the matching χ^2 distributions for correct and fake matches.

In the next step the matching candidates are fitted again, this time with the momentum constrained to the value measured in the muon spectrometer, since its momentum resolution is

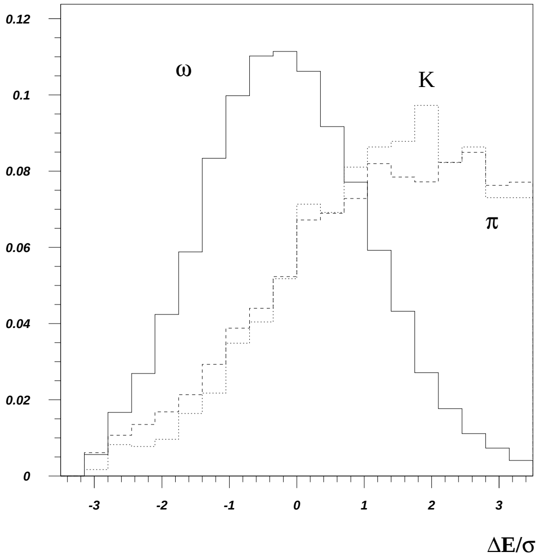

Figure 5.2: Difference between the energy of the (single) tracks measured in the vertex spectrometer and in the muon spectrometer.

better than the one of the silicon vertex telescope. This step rejects some of the fake candidates and improves the precision of the offset measurement, in the y coordinate, to $\sim 30\ \mu$m.

When the tracks reconstructed in the dimuon spectrometer are muons from π or K mesons that decayed after the pixel telescope, the vertex spectrometer measures the energy of the parent meson, which is of course always somewhat higher than the energy of the muon. Therefore, a cut on the weighted difference between the energies measured by the two spectrometers, ΔE, improves the rejection of π and K decay background. Figure 5.2 shows the simulated ΔE distribution, in units of σ, for single muons from ω, π and K decays. A cut at around 3 σ eliminates a big fraction of the background from pion and kaon decays.

There are two kinds of background in our experiment. At the trigger level we have muon pairs composed of muons coming from uncorrelated decays of pions and kaons (combinatorial background). In the final mass distribution, we also have a certain amount of events where the muon tracks were matched to a "fake" track in the vertex spectrometer.

It can be shown that the total number of opposite-sign muon pairs resulting from π and K decays is related to the corresponding like-sign numbers according to the expression $N^{+-} = 2R\sqrt{N^{++} \times N^{--}}$, where the R factor accounts for possible correlations at the level of π and K production. This factor is usually very close to unity, except in the most peripheral collisions, where the correlations among parent mesons produced in the same nucleon-nucleon interaction cannot be neglected. Its specific numerical value can be calculated by simulation and cross checked experimentally, by comparing the number of muon pairs with the different charge combinations, in several bins of the offset variable.

The background subtraction procedure consists of several steps, described in the following lines. For each centrality and kinematics bin we do the matching of single muons and fill the matching χ^2 histogram for *all* candidates. Then the same procedure is done with *mixed* events: the muons from the muon spectrometer are matched to tracks from the vertex spectrometer which belong to different events, again accounting all candidates. After normalising this sample to a single event, we get the (normalized) χ^2 distribution for *fake* matches, for each particular centrality class. Subtracting it from the first histogram we obtain the "correct matching

χ^2 distribution". This is done separately for muons from opposite-sign and like-sign triggers. Knowing the signal to background ratio, from these distributions we derive four matching χ^2 distributions: correct and fake matches for signal and background muons.

Having these distributions, and a certain cut on χ^2, we can derive the probability that the selected matched track is *correct* or *fake*, for every event with a certain number of candidates for matching. For dimuons, the probability of having a correct match is the product of the corresponding probabilities for the single muons. For every matched muon pair we can, therefore, deduce the probability that both muons are correctly matched, that one of them is incorrectly matched, and that both muons are incorrectly matched. These probabilities are then used as weights to normalise and subtract the dimuon samples of the two latter types, built with the mixed events technique.

The detailed procedure of fakes subtraction at the dimuon level is still under optimisation, in particular in what concerns the class of events where one of the tracks was correctly matched but the other is a fake. The precision of the weight calculation is only limited by the available sampling statistics, which in our case is expected to be vast.

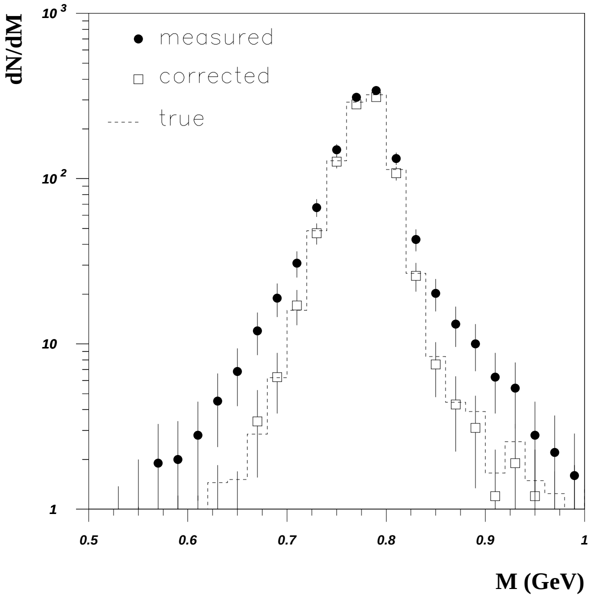

Figure 5.3: Mass spectrum for generated and matched ω's, before and after subtraction of the fake matches contamination.

An example of how the fakes subtraction works is shown in Fig. 5.3, obtained by only generating ω mesons. Besides the distributions obtained before and after subtracting the fake combinations, the figure also includes the generated distribution, as a reference.

5.3 Low mass prompt dimuons

The low mass dimuons will be studied with the "low mass" configuration, described in Section 5.1. Figure 5.4 shows the acceptances for 3 classes of dimuon mass ($M = 500$ MeV, ω and φ dimuons), as a function of the dimuon transverse momentum. The parameters that have the biggest influence on the acceptance are the field intensity of the toroidal magnet, the field in the vertex spectrometer and the hadron absorber configuration. The dipole field in the target region makes the low p_{T} muons bend into the acceptance of the muon spectrometer. This effect can be seen in the p_{T} distributions of accepted ω dimuons shown in Fig. 5.5, calculated for a current of 3000 A in the toroidal magnet and including 20 cm of iron in the muon filter. These figures reflect the influence of the TC8 dipole field on the acceptance of the muon spectrometer but do not reflect the existence of the silicon pixel telescope. In particular, no track reconstruction or matching efficiencies are included.

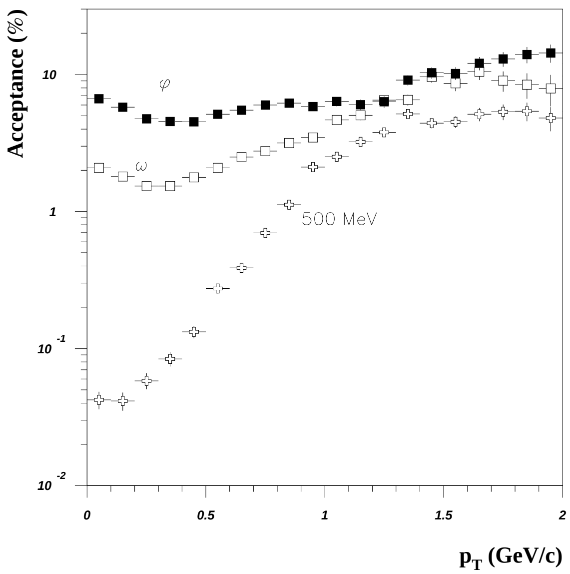

Figure 5.4: Acceptance versus dimuon p_{T} for ϕ, ω and $M = 500$ MeV dimuons, with the 1.67 T dipole field.

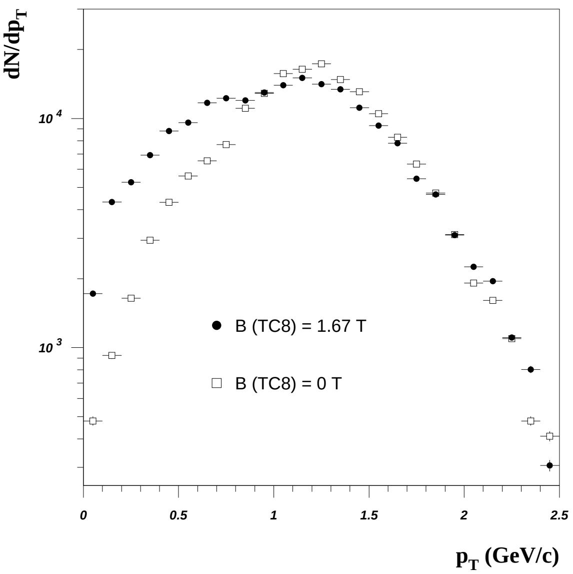

Figure 5.5: Influence of the vertex magnetic field in the p_{T} distribution of accepted ω's.

When we study low mass dimuons, only the tracks pointing to the interaction vertex are selected. Since most of the π and K decay muons have a significant offset from the interaction vertex, the combinatorial background rejection is more efficient than in the case of the open charm study. The reduced sample of matching candidates also results in a smaller contamination from fake matches. With the matching cuts tuned in our simulation, 30 % of the dimuon events produced in average Pb-Pb collisions are reconstructed and correctly matched.

Since we are looking for prompt dimuons, the pairs of matched tracks are fitted with constrained curvatures and the additional requirement of a common vertex in the proximity of the interaction point, in order to achieve the best mass resolution. Figure 5.6 shows the mass resolution for the matched dimuons, as a function of the dimuon mass. For comparison, we also show the mass resolution obtained if we only use the information provided by the muon spectrometer.

The dimuon signal mass spectrum obtained with the proposed detector layout, after subtracting the combinatorial background and fake matches, is plotted on the right side of Fig. 5.7. The background distribution (including the fake matches) is also shown. For comparison, the left side of this figure shows the corresponding spectra if the pixel spectrometer is not used. We clearly see a strong improvement in terms of mass resolution and signal to background ratio.

The statistics corresponds to one week of data taking. At a beam intensity of 10^7 ions/burst, with a target thickness of 17 % λ_{int} and a beam efficiency of 75 %, we expect to collect around 150 000 ρ, ω and ϕ events. The (statistical) errors on the signal shown in Fig. 5.7 include the contribution from the subtraction of the background.

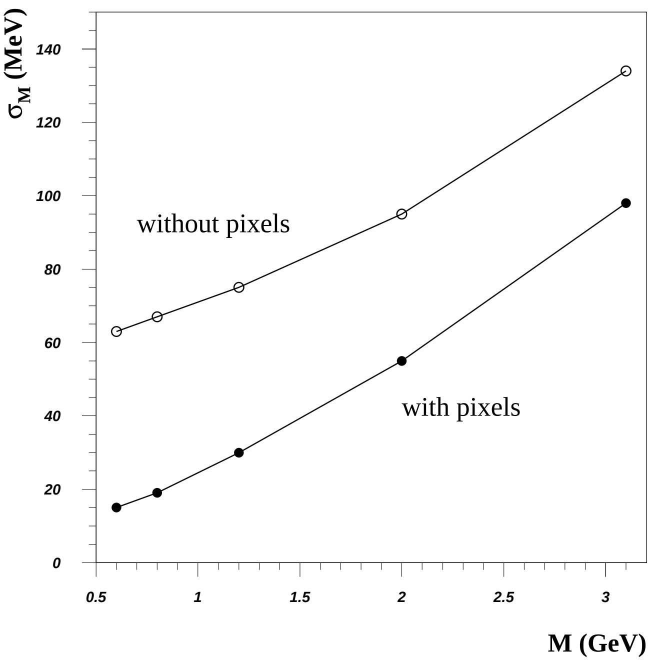

Figure 5.6: Mass resolution as a function of the dimuon mass, before and after using the pixel telescope information, for $I(ACM) = 3000$ A and with 20 cm of iron at the end of the muon filter.

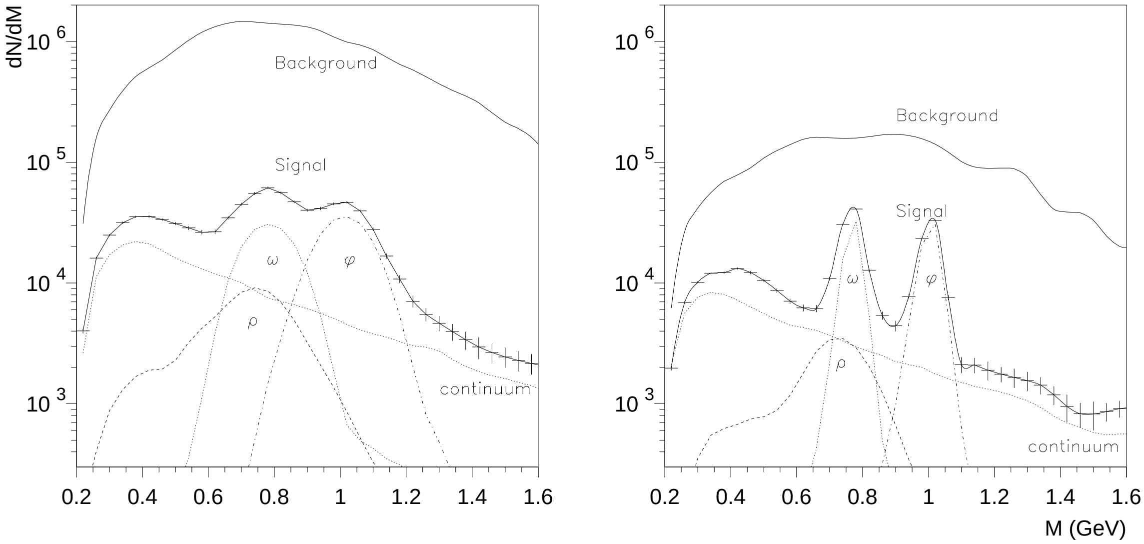

Figure 5.7: Dimuon mass distribution in Pb-Pb collisions, as measured before (left) and after (right) using the pixel telescope information. The statistics corresponds to one week of running.

The expected signal to background ratio is shown in Fig. 5.8 as a function of the mass of the muon pairs, with and without using the pixel spectrometer. We see that the signal to background ratio, an important factor in the significance of the measurements, is better than 1/5 in the region of the resonances and around 1/20 in the continuum, considering the combinatorial meson decays and the fake matches. We can appreciate the improvement due to the use of the pixel vertex spectrometer. Of course, if the Pb-Pb signal is enhanced, our signal to background ratio will be correspondingly better.

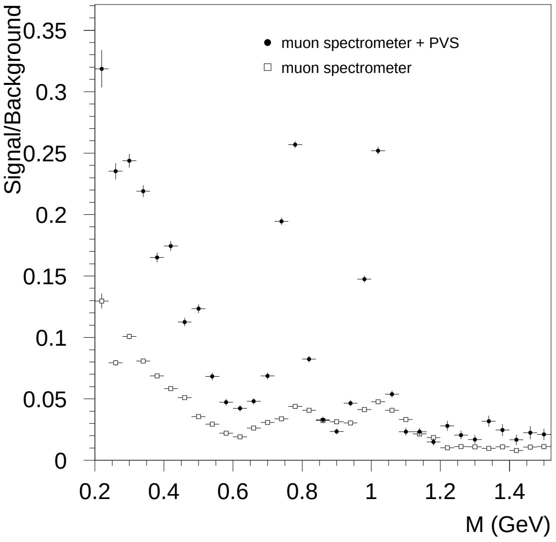

Figure 5.8: Signal over background ratio as a function of the dimuon mass.

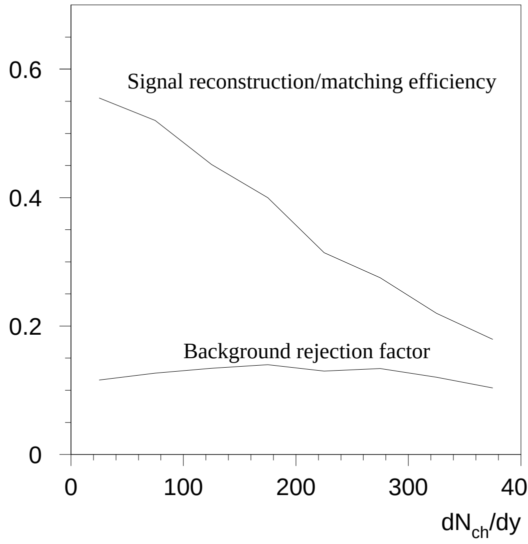

Figure 5.9: Efficiency of the track reconstruction and matching versus particle multiplicity.

Figure 5.9 shows the evolution with charged particle multiplicity of the efficiency to reconstruct and match the tracks. This evolution is partially determined by the matching criteria, which change with multiplicity to keep the level of background events under control.

As already mentioned in Chapter 2, one of the most interesting physics topics in connection with the low mass region is the possibility that the ρ line shape may change, from p-p to Pb-Pb and from peripheral to central collisions, as a consequence of in medium effects. In Fig. 5.10 we show the relative contribution of the ρ to the total expected signal, assuming that nothing exceptional happens to the shape and total yield of all contributions. One clearly observes that

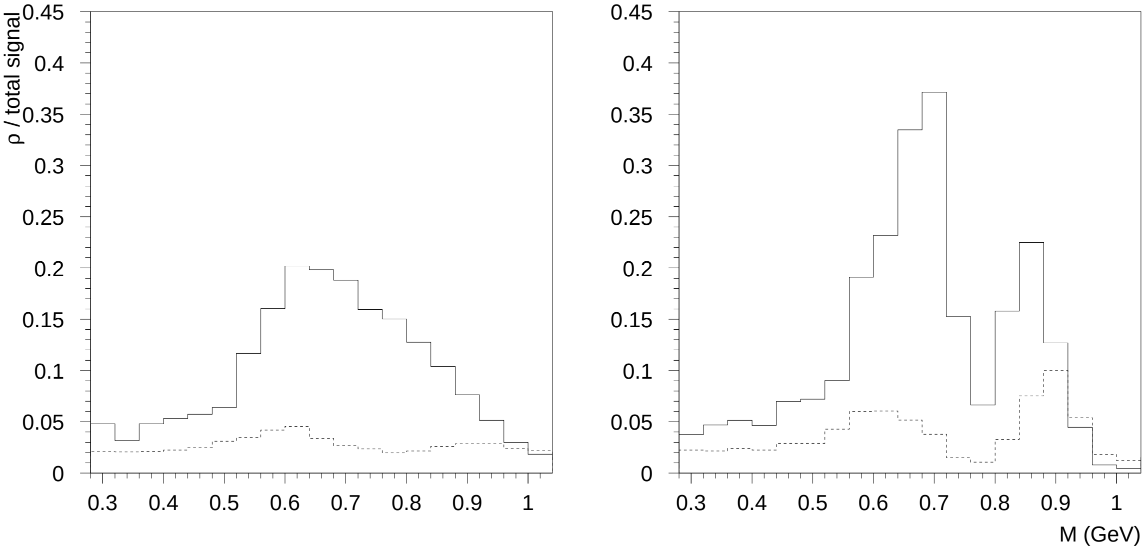

Figure 5.10: Relative contribution of the ρ to the total signal (solid line), without (left) and with (right) the pixel spectrometer. The dashed line represents the statistical errors on the total signal.

the best window to look for changes in the ρ is around 0.7 GeV, where its relative contribution reaches a level of $\sim 35\,\%$. Also indicated on this figure is the statistical accuracy with which we can extract the signal (see Fig. 5.7), also relative to the total signal. We can see that the contribution from the ρ decay in the mass window $550 < m < 900$ MeV is well above the statistical errors, confirming that we are sensitive to changes in the shape of the ρ resonance.

Out of the simulated mass spectra we can now deduce the accuracy with which we will be able to extract the particle yields. In this simple analysis we fit the reconstructed mass spectrum with two gaussian functions (representing the ω and ϕ resonances), a Breit-Wigner function (for the ρ) and an exponential function (the "continuum"). Comparing the fitted numbers to the input values injected in the event simulation, we have estimated that we can reconstruct the total yield of the ϕ (ω) with a relative accuracy of better than 5 % (10 %). Although our measurements are sensitive to changes in the shape of the ρ (as mentioned in the previous paragraph), the extraction of the absolute yield of ρ production remains rather uncertain, because of the model dependent descriptions of the continuum. The uncertainty on the yields remains dominated by systematics when we divide the event sample in eight centrality bins, for instance. With slightly improved fitting procedures, we should be able to measure the ratio ϕ/ω versus centrality with an accuracy better than 10 % in each point. Note that systematical uncertainties on the acceptance corrections cancel out in this ratio.

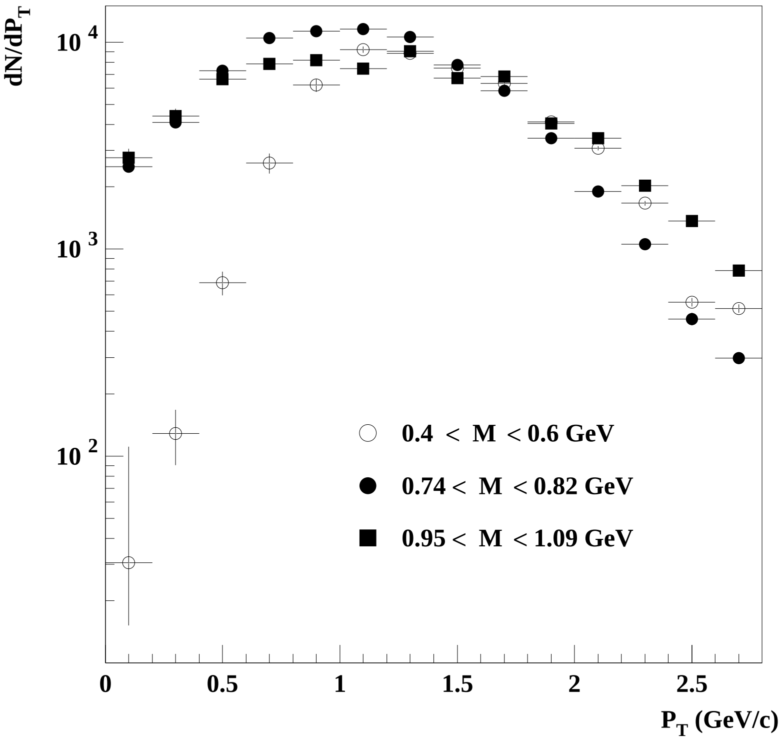

Figure 5.11: Expected p_{T} distributions for three mass windows, after one week of running.

We will be able to study the production of ω and ϕ mesons down to very small values of p_{T}, as can be seen in Fig. 5.11. On the contrary, our sensitivity to dilepton production in the mass window around 500 MeV is restricted to p_{T} values above ~ 500 MeV/c. Some modifications in the operation of the muon spectrometer (e.g., the trigger logic) would increase the acceptance for the lower values of m_{T}, but further studies are needed in that respect.

5.4 Intermediate mass dimuons

Our capability of measuring the impact parameter of the muon tracks, i.e. the minimum distance between the track and the interaction point, in the transverse plane, allows us to separate the two main contributions to the intermediate mass signal spectrum: a prompt dimuons event sample and a "displaced" muon pairs event sample, dominated by decays of *D* mesons. For the first data sample we select muon pairs where both tracks are "prompt" muons, i.e. both come from (very close to) the interaction vertex. The second data sample is built by selecting events with both muon tracks having a certain minimum offset with respect to the interaction point and a minimal distance between themselves at $z = z_{\text{vertex}}$.

This procedure allows to distinguish the contributions from prompt dimuons and from charm decays, and understand which of these signals is the origin of the experimentally observed enhancement of intermediate mass dimuons. From the "displaced tracks" event sample, we can measure the evolution with centrality of the open charm production yield.

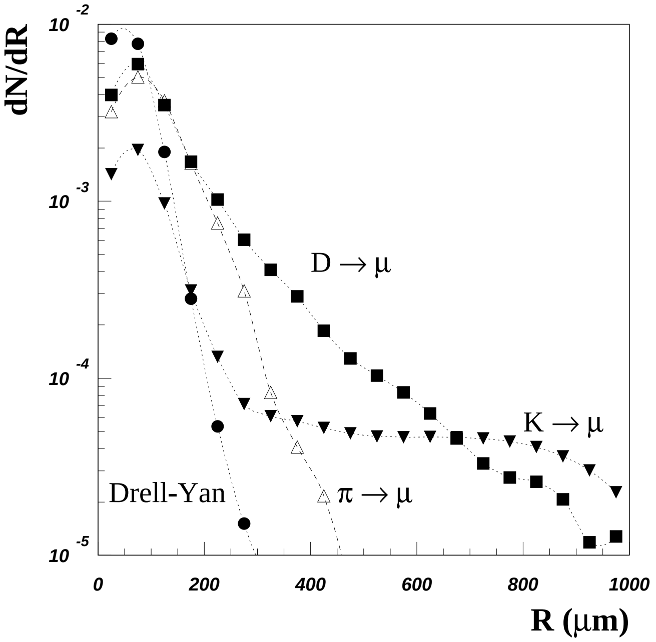

Figure 5.12: Offset distribution for accepted muons from different sources. Note that the distributions are not normalized.

Figure 5.12 shows the offset distribution of the muon tracks from the different sources. For the prompt dimuon analysis, we only accept those events where both muons cross the transverse plane at $z = z_{\text{vertex}}$ at a distance smaller than 2 times the resolution on this measurement ($2\sigma \approx 90\ \mu$m). On the other hand, the open charm event sample is composed of those events where both muon tracks have an offset larger than 1.5σ, smaller than $\sim 800\ \mu$m, and are separated from each other by more than 180 μm in the transverse plane at $z = z_{\text{vertex}}$.

While ensuring that the final data sample is dominated by muon pairs from open charm decays, the offset selection introduces a large reduction in the number of good events. The signal efficiency decreases from $\sim 15\,\%$ to $\sim 5\,\%$, when going from the most peripheral to the most central Pb-Pb collisions (see Fig. 5.13). We note that the rejection of combinatorial background is less efficient in the open charm analysis than in the prompt analysis, since the muons from π and K decays also have significant offsets.

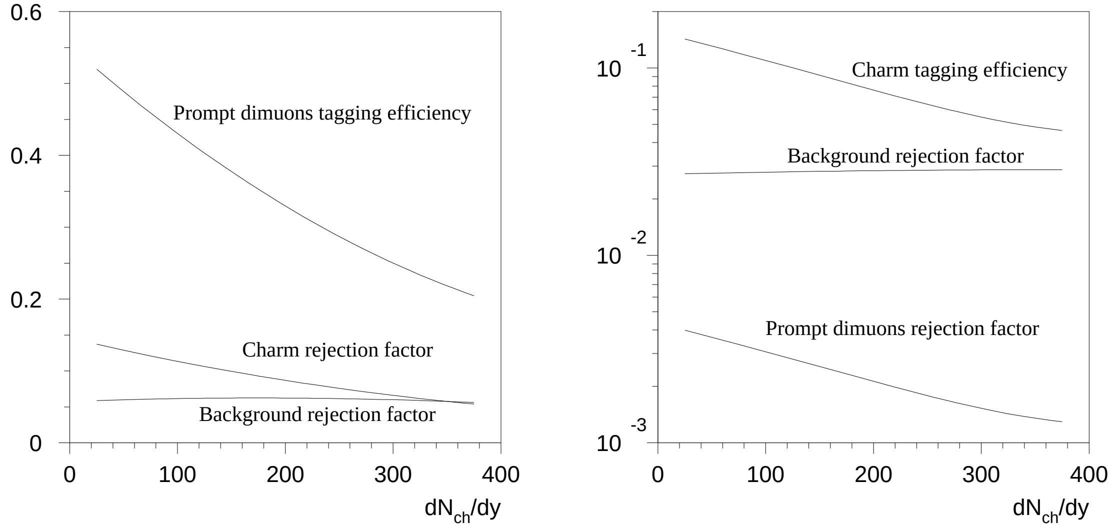

Figure 5.13: Signal selection efficiency and background rejection power for the prompt dimuons (left) and open charm (right) event samples, as a function of the number of produced charged particles.

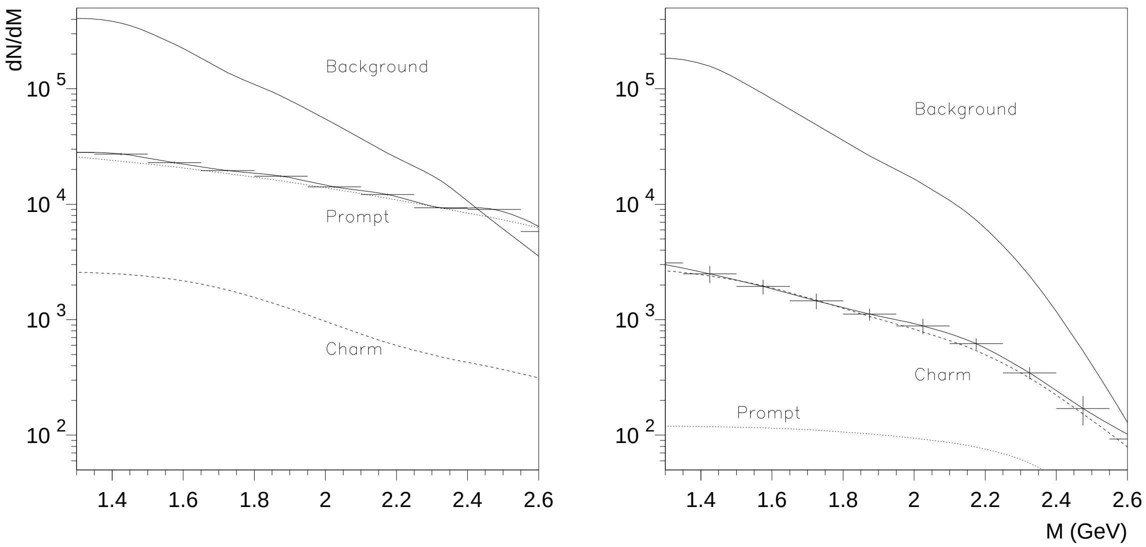

Figure 5.14: Dimuon mass distributions for the prompt (left) and charm (right) event selections.

Figure 5.14 shows the mass spectra for both the prompt dimuons (left) and open charm (right) selection. The background contribution, including π and K decays and fake matches, is also shown. These curves correspond to average Pb-Pb collisions (integrating over all centralities), taken with the “high mass” configuration described in Section 5.1. For dimuon masses above 1.2 GeV, we see that more than 90 % of the signal is due to prompt dimuons or to open charm decays, depending on the selection procedure. The corresponding signal to background ratio, in the mass range $1.2 < M < 2.5$ GeV, is 1/10 in the prompt event sample and 1/40 in the charm sample. These numbers are calculated without assuming any excess in the signal sources.

If there is an enhancement in the prompt dimuons sample, we would like to clarify whether

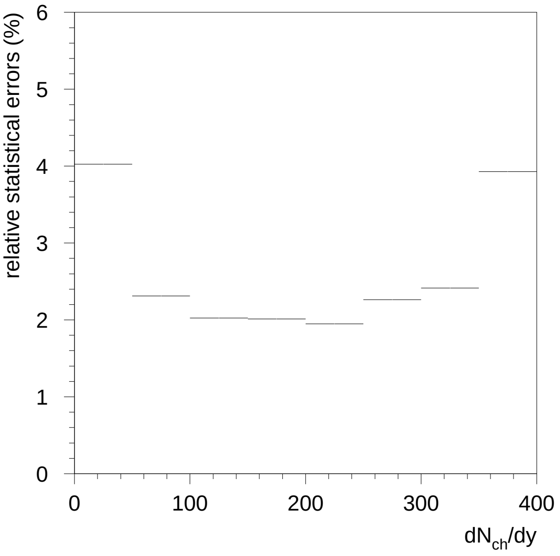

Figure 5.15: Accuracy on the centrality dependence of intermediate mass prompt dimuon production, in 8 equidistant bins.

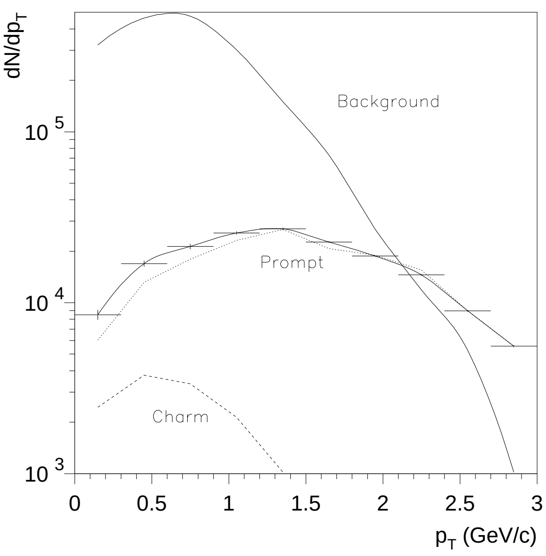

Figure 5.16: Expected p_T distribution of the intermediate mass prompt dimuons. The statistics correspond to 30 days of running.

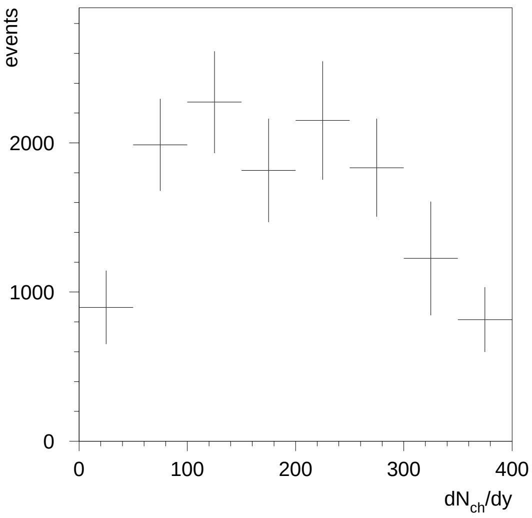

Figure 5.17: Centrality dependence of the open charm production yield, after 30 days.

it is due to the production of thermal dimuons or to changes in the Drell-Yan contribution. This study will benefit from a simultaneous analysis of the mass and transverse momentum distributions of the prompt dimuons, and from knowing how their production rate evolves with the multiplicity of charged particles emitted in the collision. Figures 5.15 and 5.16 illustrate the accuracy with which we can measure the yield of prompt dimuon production as a function of charged multiplicity and of the dimuon p_T, after one month (in the standard running conditions of the experiment). This precision should allow a good comparison with the available models.

Figure 5.17 shows the expected number of open charm events as a function of the charged particle multiplicity, after 30 days of running.

5.5 Charmonia production

With the data sample collected for the study of the open charm production yield, we can also study charmonia production and suppression. In fact, the measurement of the ψ' resonance is considerably improved by the existence of the pixel spectrometer, in view of the improved mass resolution.

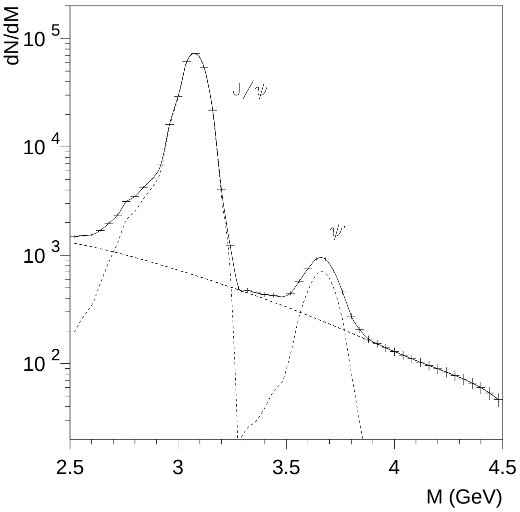

Figure 5.18: Dimuon mass distribution calculated for Ag-Ag collisions.

Figure 5.18 shows the dimuon mass distribution in the mass window of the charmonia states, as expected for average Ag-Ag collisions. When the dimuons are reconstructed using the information of the pixel spectrometer, the mass resolution is considerably improved, from ~ 90 to ~ 55 MeV in the J/ψ peak and from ~ 120 to ~ 75 MeV in the ψ' peak. This facilitates the extraction of the ψ' yield, since it becomes completely insensitive to the details with which we describe the tail of the J/ψ peak. The extraction of the ψ' yield also requires carefully subtracting the underlying continuum, for which it is very helpful to have a "continuum" window between the two peaks. These constraints lead to a more robust fitting procedure, resulting in reduced systematical uncertainties. Since the background contribution is negligible in this high mass window, the uncertainties on the measurement of the J/ψ and ψ' yields are dominated by statistics.

The statistical uncertainties presented in Fig. 5.18 were calculated for $\sim 10^{12}$ Ag-Ag collisions, assuming that the beam energy is 158 A GeV, and assuming four weeks of data collection, at 5×10^7 incident ions per burst and 75 % running efficiency. With this luminosity we should be able to have a reasonable understanding of the ψ' suppression pattern. Of course, the study of the J/ψ suppression pattern will not be limited by statistics. We should emphasise that our measurements will not be affected by unrecognized reinteractions in the targets or by Pb-air collisions, thereby allowing an accurate study of the most peripheral and most central collisions. Figure 5.19 shows the accuracy expected in the measurement of the centrality dependence of the charmonia production rates. With seven equidistant bins in $\mathrm{d}N/\mathrm{d}y$ we would measure the ψ' yield with ~ 5 % accuracy in each bin. We conclude that 30 days of Ag-Ag running would provide a detailed pattern of the J/ψ and ψ' suppression, in the region of energy density where the NA38 and NA50 experiments have shown that these resonances exhibit a peculiar behaviour.

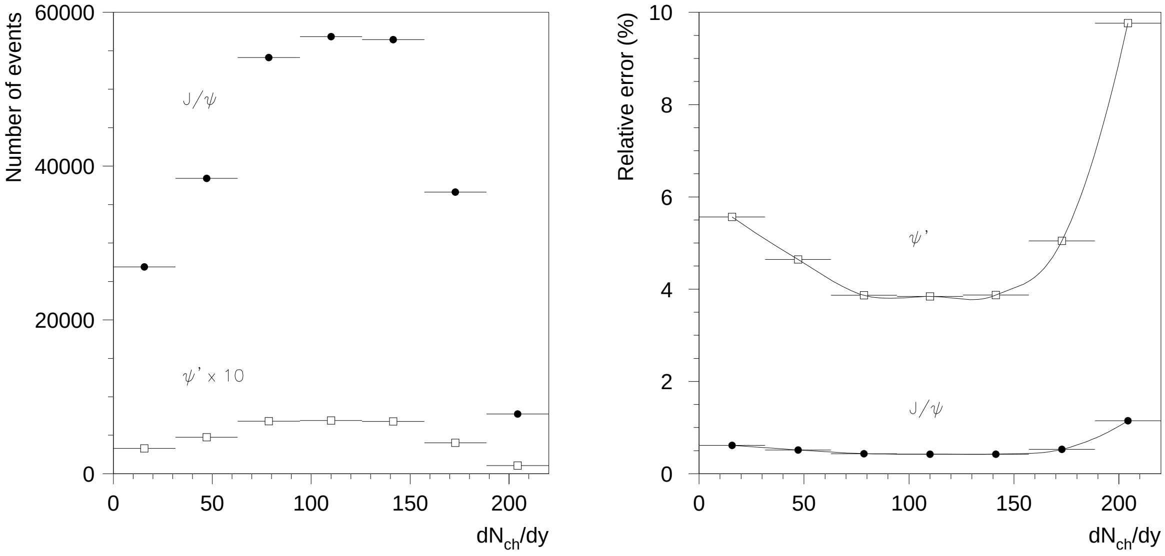

Figure 5.19: Multiplicity distributions (left) and corresponding accuracy (right) of the charmonia resonances produced in $\sim 10^{12}$ Ag-Ag collisions, without including any anomalous suppression.

5.6 A-dependence of χ_c production

As mentioned in Chapter 2, one of the goals of our experiment is the measurement of the dependence of χ_c production on the mass number of the target in p-A collisions. To minimise the systematical errors of such a measurement, we will measure the ratio between χ_c and J/ψ production and study its variation (if any) from p-Be to p-Pb collisions.

We intend to run with a system of four Be targets, of 1 mm diameter, followed by one Pb target, of 10 mm diameter, all of them being 1.5 mm thick. The targets are followed by a 0.5 mm thick Pb disk, to convert the photons, in order to detect the $\chi_c \rightarrow \psi\,\gamma \rightarrow \psi\, e^+e^-$ decays. The Pb target also works as a converter for the photons produced in the upstream Be targets.

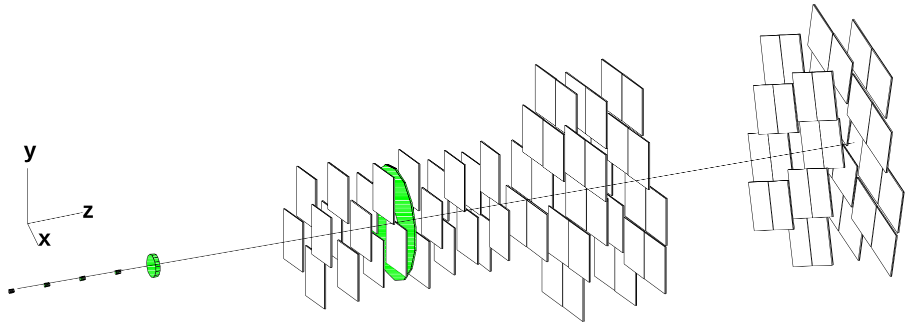

Figure 5.20: Layout of the pixel vertex spectrometer, as used in the p-A studies.

The kinematical distributions of the χ_c mesons were generated with PYTHIA and normalized to the absolute cross sections measured by the E771 Fermilab experiment [5]. The cross sections for J/ψ and ψ' production were extracted from the NA51 measurements [6]. All values were scaled to p-A collisions assuming $\sigma(pA) = \sigma(pN) \times A^{0.92}$. The resulting full phase space multiplicities per p-Pb interaction are 2.5×10^{-5}, 3.1×10^{-6}, 2.7×10^{-5} and 5.0×10^{-5}, respectively for the J/ψ, ψ', χ_{c1} and χ_{c2} charmonia states. In p-Be interactions the particle yields are two times smaller. The background was generated with the Venus event generator. All the particles were tracked through the pixel spectrometer using GEANT, taking into account all relevant processes, including δ-ray production. The resulting muons were then tracked through the hadron absorber and the muon spectrometer.

The only essential difference between the reconstruction of p-A and nucleus-nucleus data is the vertex fit procedure. In the p-A runs we do not use the beamscope detector and the number of tracks is not enough to get a good resolution on the vertex. Still, the z-vertex resolution in p-A interactions is good enough (~ 1 mm) to identify the subtarget where the interaction took place. Therefore, in the p-A analysis we fit the vertex only to identify the target and then fit the x and y coordinates of the vertex assuming that the interaction took place in the centre of the target. This results in a resolution of ~ 40 and ~ 50 μm in the x and y vertex coordinates, respectively.

When looking for $\chi_c \rightarrow \psi\,\gamma \rightarrow \psi\, e^+e^-$ decays, the event reconstruction and selection proceeded through the following steps. For each event, all the tracks with fitted momentum above 500 MeV/c and at least four hits were reconstructed. A very loose constraint on the offset of the track at the target centre was used. (5 mm instead of the usual ~ 0.2 mm). After matching the muons to tracks in the pixel spectrometer with the usual procedure, the candidate tracks giving a dimuon mass in the range 2.7–3.4 GeV were refitted with the mass constrained to the J/ψ mass. The reconstruction and matching efficiency after all the cuts was $\sim 80\,\%$ for J/ψ dimuons. The opposite-sign pairs of the remaining tracks with $M < 50$ MeV were refitted with the requirement of a common vertex, either on the target or on the photon converter disk, and $M = 2\ m_e$. After applying various selection cuts, the pair with smallest χ^2 of dielectron fit was chosen as candidate for the converted γ. An additional cut $p_{\mathrm{T}}(e^+e^-) > 250$ MeV/c was applied, to reduce the background.

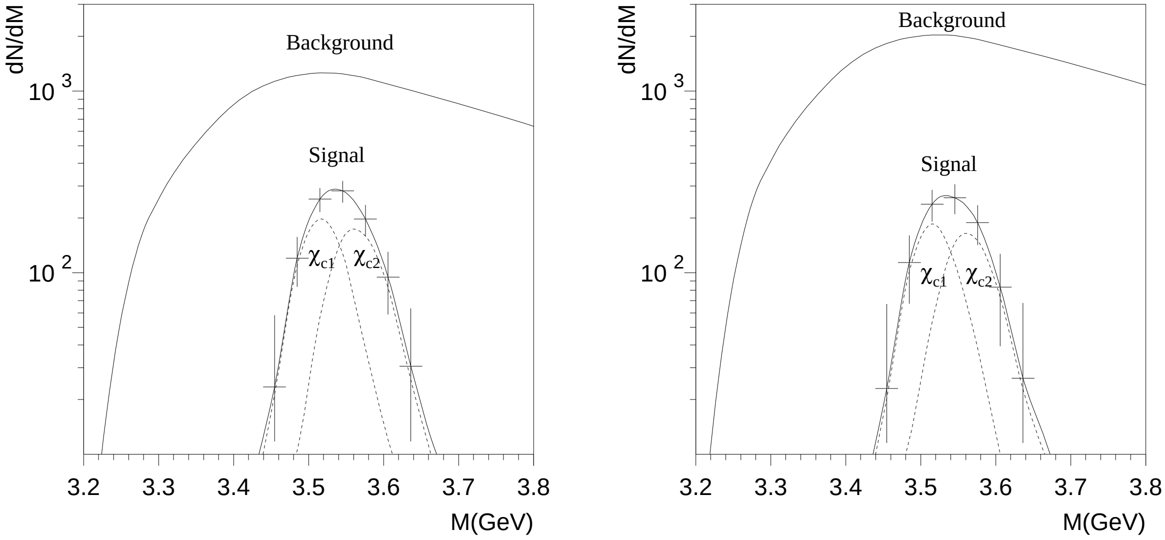

Figure 5.21: $\psi\, +\, e^+e^-$ invariant mass distribution, for the signal and the background, for 2×10^{12} p-Be (left) and 1.2×10^{12} p-Pb (right) interactions.

Figure 5.21 shows the corresponding signal and background mass spectra, for p-Be and p-Pb interactions. The background can be subtracted with mixed events, combining the J/ψ with an e^+e^- pair of different collisions.

For $\chi_c \rightarrow \psi\,\gamma$ events where the J/ψ is triggered by the muon spectrometer, 7.5 % of the photons convert in the Pb target and 5 % in the converter. The efficiency of e^+e^- pair reconstruction is $\sim$43 %, leading to a total reconstruction efficiency of such events of $\sim$5 %. The mass resolution is 32 and 34 MeV for the χ_{c1} and χ_{c2}, respectively.

In order to estimate the background, the invariant mass spectrum of the J/ψ and e^+e^- candidates, from different events, was weighted with the probability of the J/ψ trigger (regardless of the origin of the J/ψ).

With four 1.5 mm thick targets of Be and one of Pb, using a proton beam of intensity around 10^9 protons per burst, and assuming a running efficiency of about 75 %, we can expect to collect in 4 weeks $\sim$950 χ_c events in p-Be and $\sim$900 in p-Pb collisions. The background in the mass range $3.47 < M < 3.63$ GeV is $\sim$6000 and 9800 events for the p-Be and p-Pb samples, respectively.

5.7 Intermediate mass dimuons in p-A collisions

Using the same data sample as used in the χ_c studies, we will study the production of open charm in p-Be and in p-Pb collisions. Figure 5.22 shows the expected mass distribution of the intermediate mass dimuons in the open charm event selection mode. The statistical accuracy corresponds to a run of 30 days with four Be targets followed by a Pb target, each of them 1.5 mm thick. A very similar figure is obtained from the p-Pb data.

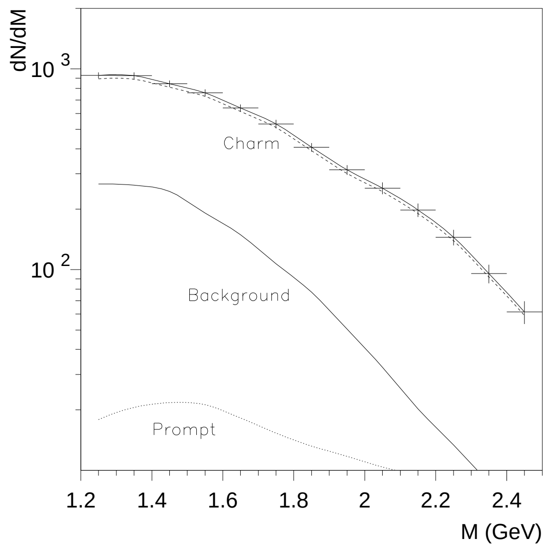

Figure 5.22: Intermediate mass dimuons in the open charm event selection mode, collected in p-Be collisions after 30 days.

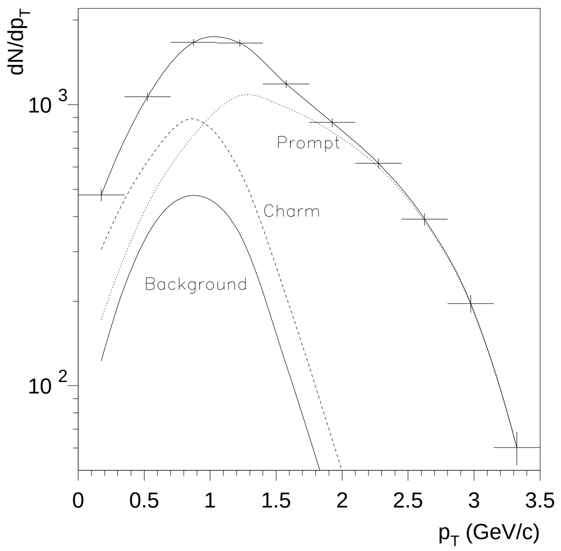

Figure 5.23: p_T distribution of the intermediate mass prompt dimuons collected in p-Be collisions, after 30 days of running.

We will also study the production of intermediate mass prompt dimuons in proton induced collisions. Figure 5.23 shows the expected p_T distribution of the intermediate mass dimuons ($1.2 < M < 2.6$ GeV) in the “prompts” event selection mode, in the same running conditions. Once again, the p-Pb collisions lead to a very similar figure.

The statistical precision of these measurements will allow to make a very accurate measurement of the ratio between the open charm and the Drell-Yan production cross sections (at the few % level), in each p-A collision system. Therefore, we will be able to clarify if these two hard processes have the same A-dependence or not. The accuracy of this study will be limited by systematical uncertainties due, for instance, to the isospin dependence of the Drell-Yan cross section or to the uncertainties in the nuclear effects on the gluon distribution functions.

Furthermore, Fig. 5.23 shows that we will make a very clean measurement of prompt dimuons with a transverse momentum higher than half their mass (1.3 GeV/*c* or less). The very small background in this measurement makes it very competitive with respect to the currently available data on real photon production, providing a good source of information on the gluon density functions.

6 Organization and Planning

This chapter presents the organizational details of the project, including the structure of the collaboration, the sharing of responsibilities, the planning of the future activities, and our beam time needs.

6.1 Overall structure of the project

An overview of the organisation of our project is given in Fig. 6.1, where we can see the different sub-projects and the overall assignment of responsibilities, including the list of institutes involved.

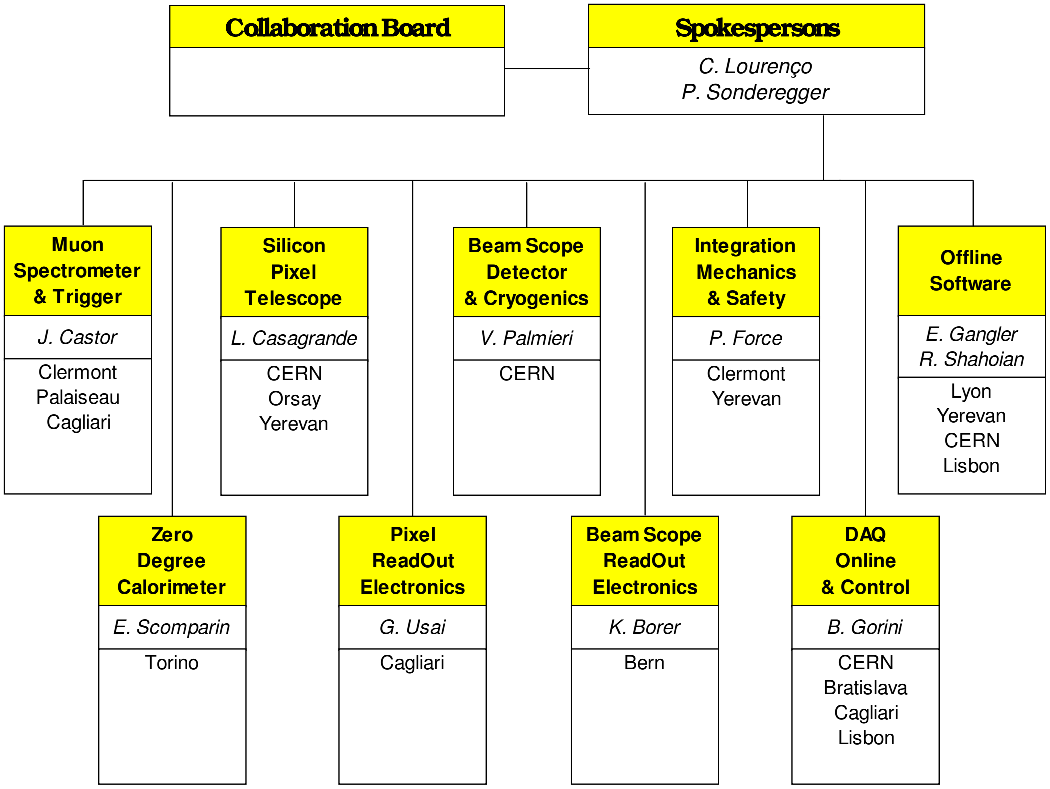

Figure 6.1: Overall structure of the project.

Of the present NA50 detectors, we will keep the muon spectrometer, essential for muon identification and trigger selectivity, and the zero degree calorimeter, which is being rebuilt. These two detectors will be used as they are today, up to their (VME) read-out electronics. The Palaiseau and Clermont-Ferrand groups will operate the muon spectrometer (detectors and electronics), with the support of the Cagliari group in what concerns the trigger hodoscopes. The Torino group will operate the ZDC.

The two new detectors, the beamscope and the silicon pixel telescope, are located in the target area, between the end of the beam line and the start of the hadron absorber, inside a dipole magnet. The magnet, named TC8, exists and has already been used in the feasibility tests done in 1998.

A prototype of the beamscope has already been built and tested, in collaboration with the RD39 group. The CERN group assumes the responsibility for the detectors, PCBs and associated cryogenics. Minor changes will be made on the detector mask geometry (longer strips). The Bern group has built and will operate the readout electronics. The online part (acquisition, monitoring and slow control) has already been done for the prototype tests and will be adapted (by Bratislava and CERN) for the final system.

The silicon pixel telescope will be built by the CERN and Orsay groups. It uses 88 Alice1 readout chips (720 000 channels), bump bonded to single-chip or double-chip sensor layers. The design, production and testing of these units is being done in collaboration with the ALICE experiment, which uses the same basic elements in its silicon pixel layers. The production of the readout chips will be done by IBM, the sensor wafers will be produced by Canberra and the bump bonding will be done by GEC-Marconi. Our own work will consist in testing the products delivered, prepare our own assemblies (arrays, planes), and establish the working conditions of the detectors before placing them in the beam. The settings for each pixel of each chip will be stored in a data base, for the “pixel calibration and control” during the physics runs. This system will be set up by the Bratislava group.

We will build the planes of the telescope by mounting the detector units on support/bus ceramics, designed in Yerevan (as was the case for the feasibility tests) and produced in CERN workshops. We plan to use gas cooling. These two issues are currently under the responsibility of the CERN and Yerevan groups. Provided we find the required resources, we will study alternative options (carbon fibre support structures, two-phase evaporative cooling). The Cagliari group takes care of the readout electronics of the pixel detector, transferring the data from the pixels, via VME, into the data acquisition system. The Clermont group is willing to design the mechanical support of the new detectors, in close collaboration with the CERN and Yerevan groups. From our feasibility tests we know that this is a critical aspect of the project, involving the mechanical assembly of the pixel planes with 100 μm positioning precision and the integration of the targets and beamscope detectors, in vacuum, at the end of the beam pipe.

The new DAQ system will read the data from the VME crates, build the events from the data streams coming from the muon spectrometer, ZDC, pixels and beamscope, monitor the data quality, and write the selected events in permanent data storage (using central data recording). For the online software we will adopt the DATE framework, developed by the CERN ALICE DAQ group and used in the NA57 experiment and in the ALICE test beam activities. This is a state of the art software package, providing all the required functionalities. The work needed to adapt this general environment to our specific case, will be done by people from the CERN, Bratislava, Cagliari and IST groups, with the support of the DATE development team.

In what concerns the offline software, the amount of data from the pixel telescope, more than 700 000 channels, and the rather demanding issue of track reconstruction and matching with very high multiplicities has imposed a radical change in the offline software framework, away from the 20-year old Fortran-Patchy-EPIO environment of NA50. We will use the AliRoot framework, an object oriented software environment developed in C++ and using Root, developed by the ALICE collaboration. Although the physics performance simulations done so far are still using Fortran codes, we have already started developing our AliRoot based software. This work is shared between the Lyon, Yerevan, CERN and IST groups.

The proposed sharing of responsibilities in the construction and testing of the components specific of this experiment is summarized in Table 6.1. Palaiseau and Torino will participate in the operation of the already existing detectors. All institutes will jointly participate in the data taking activities and data analysis.

Table 6.1: Sharing of responsibilities for the new detectors.

Item	Institutes
Silicon pixel telescope (detectors, support/bus, cooling, etc)	CERN, Orsay, Yerevan
Pixel readout electronics	Cagliari
Beamscope detector (detector, PCBs, support, cryogenics)	CERN
Beamscope readout electronics	Bern
Mechanics and integration	Clermont-Ferrand, Yerevan
DAQ, online and control	CERN, Bratislava, Cagliari, Lisbon

Table 6.2 presents the estimated cost for the different items that must be developed for this experiment. The running of the experiment requires a budget of the order of 100 kCHF per year, mostly devoted to the maintenance of the dimuon spectrometer (electronics pool, gas, etc.). We should emphasise that the detectors presently available in NA50 and to be reused in our experiment (muon spectrometer, ZDC, trigger electronics, etc.) are certainly worth more than 15 MCHF, more than 20 times the budget needed for the new investments.

Table 6.2: Cost estimate for the new detectors, in kCHF.

Item	Cost
Silicon pixel telescope	350
Pixel readout electronics	40
Beamscope detector	35
Beamscope readout electronics	65
Mechanical supports	40
DAQ, online and control	50
Total	580

6.2 Planning of activities and beam time requests

The design of the Alice1 pixel readout chip has suffered successive delays in the last year and has not yet been submitted for production. It is currently foreseen that the “engineering run” will be finished by end of June 2000. Six wafers will be produced. A series of tests will then be started, to verify the proper functioning of the chips. The production of the sensor wafers will be ready by the same time. The bump bonding procedure should start around September and we expect that it will take a few months before reaching a good yield of fully working bump bonded detectors. If these chips are seen to comply with the specifications, the “production run” (of 48 wafers) can be launched before the end of year 2000. The evaluation and optimisation of the bump-bonding techniques will be started on a set of low-cost dummy wafers, produced in the same technology as the Alice1 chip, expected to be delivered in May. This should allow a more efficient optimisation of the bump bonding procedure with the real chip wafers.

We request two weeks of proton beam during year 2001, to commission the new detectors and collect enough events to have a first run through the complete online and offline data processing chain. Since the charged particle multiplicities in p-A collisions are quite low, we should be able to do a first study of the physics of low mass dimuon production, in p-Be and p-Pb collisions, within the 2001 proton beam period. These studies can be performed with a partial azimuthal coverage of the dimuon acceptance, as we have shown in April 1998, with a layout that would require $\sim$30 Alice1 chips.

The more challenging measurements of open charm and charmonia production (production cross sections lower than the low mass dimuons) in heavy ion collisions (much higher particle multiplicities) require a fully operational silicon pixel telescope (10 planes, 88 chips). We want to do these studies in 2002 and 2003, running one week on the low mass dimuons setup, followed by four weeks in the charm configuration.

Given the very high importance we attribute to the understanding of the mechanisms responsible for the observed charmonia suppression, we want to concentrate the 2002 heavy ion run on the measurement of Ag-Ag collisions. Accelerating the Ag beam to 158 GeV per nucleon will minimize systematic uncertainties in the comparison to the Pb-Pb data, and should allow for a longer spill, which would improve luminosity. To complete our studies of low mass dilepton and charm production in heavy ion collisions, we need a second run, in 2003, with five weeks of Pb-Pb collisions at 158 A GeV.

We stress that our experiment will also be able to do very relevant “proton physics”, as already mentioned in this proposal. The capability of our experiment to measure the A-dependence of χ_c production, for instance, has been documented in the previous chapter. The corresponding measurements of open charm production rates have also been properly studied. We will also be able to provide a good measurement of high p_T (intermediate mass) prompt dimuons. Other interesting physics topics will be evaluated in the near future, including the possibility of measuring the beauty production cross section in proton (and pion) induced collisions, at $\sqrt{s} = 20$–30 GeV, via the tagging of displaced J/ψ’s. These measurements justify requesting a beam time of the order of one month per year, of 400 or 450 GeV protons, during the lifetime of the experiment. Besides these physics runs, we will also need one week of proton beam immediately before the ion runs, for setting up the experiment.

References

Chapter 1

[1] P. Braun-Munzinger and B. Müller, Summary report on “Heavy Ion Physics at the SPS”, Chamonix, Sept. 1998; http://www.cern.ch/HIPS/status_rep.ps
[2] QM’99 Conf. Proc., Nucl. Phys. **A661** (1999).
[3] http://www.cern.ch/CERN/Announcements/2000/NewStateMatter/science.html

Chapter 2

[1] G. Agakichiev *et al.* (CERES Coll.), Phys. Lett. **B422** (1998) 405.
B. Lenkeit *et al.* (CERES Coll.), Nucl. Phys. **A661** (1999) 23c.
[2] E. Anderson *et al.*, Phys. Lett. **B449** (1999) 401.
F. Antinori *et al.*, Nucl. Phys. **A661** (1999) 130c.
[3] M.-P. Comets *et al.* (NA50 Coll.), PANIC 99, XVth Particles And Nuclei International Conference, Uppsala, Sweden, June 1999.
[4] M.C. Abreu *et al.* (NA38/50 Colls.), Euro. Phys. J. C, in print; CERN-EP-2000-012.
[5] R. Rapp and E. Shuryak, hep-ph/9909348.
[6] A.L.S. Angelis *et al.* (HELIOS-3 Coll.), Euro. Phys. J. C, in print; CERN-EP / 98-92.
[7] L. Capelli *et al.* (NA50 Coll.), Workshop on Charm Production in Nucleus-Nucleus Collisions, CERN, Dec. 1999; http://www.cern.ch/HIPS/charm/dec99/na50/
[8] M.C. Abreu *et al.* (NA38 Coll.), Phys. Lett. **B466** (1999) 408.
[9] D. Kharzeev, M. Nardi and H. Satz, BI-TP-97-33, July 1997, hep-ph/9707308.
M. Nardi and H. Satz, Phys. Lett. **B442** (1998) 14; hep-ph/9805247.
[10] E.L. Berger, L.E. Gordon and M. Klasen, Phys. Rev. **D58** (1998) 074012.
[11] M.C. Abreu *et al.* (NA38/50 Colls.), Euro. Phys. J. C, in print; CERN-EP / 99-112.
[12] M.C. Abreu *et al.* (NA50 Coll.), Phys. Lett. **B**, in print; CERN-EP-2000-013.
[13] M.J. Leitch *et al.* (E866 Coll.), LA-UR-99-5007, nucl-ex/9909007.
[14] L. Antoniazzi *et al.* (E705 Coll.), Phys. Rev. **D49** (1994) 543.
[15] T. Alexopoulos *et al.* (E771 Coll.), hep-ex/9908010.

Chapter 3

[1] W. Snoeys et al., Nucl. Instr. and Meth. in Phys. Res. A 439 (2000) 349-360
[2] M. Campbell et al., IEEE Trans. on Nucl. Sci. 46-3 (1998) 156.
[3] RD39 Status Report, CERN/LHCC 2000-010, January 2000.

Chapter 4

[1] V.G. Palmieri *et al.*, Nucl. Instrum. Meth. **A413** (1998) 475.

[2] ALICE Collaboration, CERN/LHCC 99-12, ALICE TDR 4, 18 June 1999.
[3] M. Campbell et al., IEEE Trans. on Nucl. Sci. 46-3 (1998) 156.
[4] "IEEE Standard Test Access Port and Boundary-Scan Architecture", IEEE Std 1149.1–1990 (Includes IEEE Std 1149.1a–1993).
[5] RD48 Collaboration, CERN/LHCC 2000-009, LEB Status Report/RD48, Dec. 1999.
[6] T. Grassi, "Development of the digital read-out system for the CERN Alice pixel detector", PhD Thesis, Padova University, Dec. 1999.
[7] R. Arnaldi *et al.*, Nucl. Instrum. Meth. **A 411** (1998) 1.
[8] P. Gorodetzky et al., Nucl. Instr. and Meth. A 361 (1995) 161.
G. Anzivino et al., Nucl. Instr. and Meth. A 357 (1995) 380.
E. Chiavassa et al., Nucl. Instr. and Meth. A 367 (1995) 267.
[9] K. Werner, Phys. Rep. **232** (1993) 87.
[10] L. Anderson *et al.* (NA10 Coll.), Nucl. Instrum. Meth. **223** (1984) 26.
[11] ALICE Internal Note 1999-46.
http://consult.cern.ch/alice/Internal_Notes/1999/46/abstract

Chapter 5

[1] C. Cicalò *et al.*, CERN/SPSC 99-15/I221, Letter of Intent to the CERN SPSC.
[2] T. Sjöstrand, Comp. Phys. Comm. **82** (1994) 74.
http://www.thep.lu.se/t̃orbjorn/Pythia.html
[3] A.D. Martin, R.G. Roberts and W.J. Stirling, Phys. Rev. **D51** (1995) 4756.
[4] K. Werner, Phys. Rep. **232** (1993) 87.
[5] T. Alexopoulos *et al.* (E771 Coll.), hep-ex/9908010.
[6] M.C. Abreu *et al.* (NA51 Coll.), Phys. Lett. **B438** (1998) 35.

Printed at CERN